Endothermic Charge Separation Occurs Spontaneously in Non-Fullerene Acceptor/Polymer Bulk Heterojunction

Kushal Rijal,[1,*] Neno Fuller,[1] Fatimah Rudayni,[1,2] Nan Zhang,[3] Xiaobing Zuo,[4] Cindy L. Berrie,[5] Hin-Lap Yip,[3,6,7] Wai-Lun Chan[1,*]

1. Department of Physics and Astronomy, University of Kansas, Lawrence, Kansas 66045, USA
2. Department of Physics, Jazan University, Jazan 45142, Saudi Arabia
3. Department of Materials Science and Engineering, City University of Hong Kong, Tat Chee Avenue, Kowloon, Hong Kong
4. X-ray Science Division, Argonne National Laboratory, Lemont, Illinois 60439, USA
5. Department of Chemistry, University of Kansas, Lawrence, Kansas 66045, USA
6. School of Energy and Environment, City University of Hong Kong, Tat Chee Avenue, Kowloon, Hong Kong
7. Hong Kong Institute for Clean Energy, City University of Hong Kong, Tat Chee Avenue, Kowloon, Hong Kong

Abstract:

Organic photovoltaics (OPVs) based on non-fullerene acceptors (NFAs) have achieved a power conversion efficiency close to 20%. These NFA OPVs can generate free carriers efficiently despite a very small energy level offset at the donor/acceptor (D/A) interface. Why these NFAs can enable efficient charge separation (CS) with low energy losses remains an open question. Here, the CS process in the PM6:Y6 bulk heterojunction (BHJ) is probed by time-resolved two-photon photoemission (TR-TPPE) spectroscopy. We found that the CS, the conversion from bound charge transfer (CT) excitons to free carriers, is an endothermic process with an enthalpy barrier of 0.15 eV. The CS can occur spontaneously despite being an endothermic process, which implies that it is driven by entropy. We further argue that the morphology of the PM6:Y6 film and the anisotropic electron delocalization restrict the electron and hole wavefunctions within the CT exciton such that they can primarily contact each other through point-like junctions. This configuration can maximize the entropic driving force.

* Email: kushalko85@ku.edu, wlchan@ku.edu

1. Introduction

Fullerene and its derivatives have long been used as the electron acceptor in organic photovoltaics (OPVs). However, despite decades of research and optimization, the efficiency of fullerene based OPVs plateaued at ~ 12% in the early 2010s,[1] which was significantly lower than the efficiency of photovoltaics made with other materials such as silicon and halide perovskites. This paradigm is shifted by the recent introduction of the Y-series non-fullerene acceptors (NFA), which results in a rapid increase in the OPVs efficiency towards ~ 20% in just a few years.[2-11] In high performing NFA/polymer bulk heterojunctions (BHJs), free carriers can be generated efficiently even when the energy offset between the singlet (S_1) exciton in the NFA and the charge transfer (CT) exciton is as small as ~0.1 eV, [12-15] which significantly reduces the energy loss from the initial CT process at the donor/acceptor (D/A) interface. By contrast, for fullerene/polymer BHJs, a much larger energy offset (> 0.3 eV)[1, 16] is often required to produce a high charge separation (CS) yield. Moreover, NFA based OPVs generally have a lower non-radiative recombination loss compared to fullerene based OPVs,[14, 17, 18] which can be attributed to the long carrier lifetime found in NFA/polymer BHJs.[9, 19] The low energy losses in both initial CT and charge extraction processes lead to a high open circuit voltage and the record-breaking power conversion efficiency.

While various mechanisms, such as the inhibition of triplet formation,[9, 20] have been proposed to explain the long carrier lifetime in NFA OPVs, it is less clear why free carriers can be generated efficiently in the first-place despite the very small S_1-CT energy offset. It is known that an electron-hole pair at the D/A interface is bound together to form a CT exciton, which can has a binding energy as large as ~0.5 eV.[21-23] Electron/hole delocalization would reduce this binding energy by forming the so-called hot CT excitons.[24-27] However, when the energy offset at the D/A

interface is small, the initial CT transfer process cannot provide enough excess energy to populate such hot CT excitons, and CS needs to proceed *via* more localized and bound cold CT excitons. Mechanisms that allow the dissociation of cold CT excitons often rely on the extraction of electrons/holes by some lower energy sites originated from interfacial molecular mixing,[28-32] energetic disorders,[33, 34] or polaron formation.[35] These lower energy sites provide a gradient in the potential energy counteracting the CT exciton binding energy, but they unavoidably lead to a decrease in the potential energy of the separated carrier. Hence, these mechanisms intrinsically lead to energy losses. While details for each of these mechanisms can be very different, a simplistic view is that if a CT exciton is bound, one must pay the energy price to separate it into free carriers. Hence, it is counterintuitive that OPVs consisting of NFAs seemingly defy this basic rule and produce free carriers at a much lower energy loss.

In this work, we investigate the CS process in a representative NFA/polymer blend that is known as the Y6/PM6, which was responsible for the breakthrough in the OPV efficiency from ~12% to ~16%. We note that this NFA/polymer blend has been investigated previously by time-resolved optical pump-probe spectroscopy.[19, 36-39] Here, time-resolved two photon photoemission spectroscopy (TR-TPPE) is employed, which allows us to measure the energy of the excited electron directly. By using this technique, we can trace the energy of the excited electron as a function of time during the CS process, which has not been captured by previous spectroscopy works. We found that CT excitons are generated within the first few picoseconds after the initial photoexcitation. Then, we observe a bifurcation of the CT exciton population into a higher energy charge separated state, and a lower energy trapped state. The CS process results in an enthalpy increase of ~ 150 meV. This observation is rather uncommon because excited electrons typically

lose energy to the environment instead of gaining energy from it. The observed enthalpy-uphill CS is also opposite to the typical hot exciton cooling observed in fullerene D/A interfaces.[24-26, 40]

Our samples do not have any electrode for carrier extraction. Under this condition, excited electrons typically relax from higher energy states to lower energy ones as they equilibrate with the environment. Hence, the transfer of electrons from a lower to a higher energy state is counterintuitive. Indeed, by the principle of detailed balance, the steady-state population of the higher energy CS state should be orders of magnitude lower than that of the lower energy CT exciton state if we assume an energy difference of 0.15 eV. We propose that the endothermic CS process is driven by entropy. When the entropic driving force can compensate for the enthalpy increase, an endothermic process can proceed as if it is an energy downhill process. An entropy-driven CS process is also consistent with the athermal charge generation observed in NFA OPVs.[41] The entropy-driven CS allows excitons to gain energy from the environment, which can intrinsically reduce energy loss compared to other CS mechanisms. We note that entropy-driven CS has been discussed in previous works,[22, 42-44] but it remains unclear on what conditions the entropy mechanism can become dominant. Based on our recent works on model D/A interfaces,[45, 46] and structural characterizations on PM6:Y6 BHJs, we will argue that the entropy driving force can be maximized in PM6:Y6 BHJs or other NFA BHJs with similar structural characters.

2. Results and Discussion

Before discussing our TR-TPPE results, we first establish the band alignment at the PM6:Y6 interface. Neat PM6 and Y6 films, and PM6:Y6 blends were spin-coated onto PEDOT:PSS/ITO substrates. The highest occupied molecular orbital (HOMO) of these samples is determined by ultraviolet photoemission spectroscopy (UPS). The UPS spectra for the three samples are shown in Fig. 1a. The energy in all the spectra is referenced with respect to the vacuum

level (E_v), in which the work function for each sample is determined from the secondary electron cutoff (SECO) of the spectrum (Fig. S1 in the supporting information). The HOMO peak is labelled in Fig. 1a. To determine positions of the HOMO's peak and rising edge more precisely, we also subtract the inelastic photoelectron background from the spectrum (the subtracted spectra are provided in Fig. S2 in the supporting information). The position of the HOMO's rising edge and the work function are used to determine the ionization potential (IP). We found that our neat PM6 and Y6 films have an IP of 5.22 eV and 5.48 eV, respectively. The IPs reported in the literature[15, 47-49] are typically in the range of 5.1 – 5.5 eV for PM6, and around 5.6 eV for Y6. Hence, our IP values show a reasonable agreement with the literature.

To a first approximation, the HOMO offset at the PM6:Y6 interface is equal to the difference in the IPs of the two materials.[50] Using this approach, we find a HOMO offset of ~ 0.26 eV. However, simply aligning the vacuum level of the two materials cannot give an accurate HOMO offset. As shown in some recent works,[47, 48, 51] when PM6 and Y6 form an interface and their Fermi levels equilibrate with each other, an interfacial dipole can develop. This can create a vacuum level offset of ~ 0.15 – 0.2 eV for PM6:Y6,[48] which can reduce the HOMO offset. Therefore, the HOMO offset determined by the IPs of neat PM6 and Y6 films tends to be large (~ 0.5 eV).[51] Indeed, other methods often find a smaller HOMO offset (~0.1 – 0.3 eV),[2, 52, 53] Our subsequent discussion does not rely on an accurate value of the HOMO offset, we will assume a HOMO offset of ~ 0.2 eV, based on the range of HOMO offsets reported in the literature. We also measure the UPS spectrum for the PM6:Y6 BHJ samples. However, we are not able to resolve the two different HOMO peaks in the BHJ films (the black curve in Fig. 1a). For the BHJ film, although the BHJ's spectrum resembles more closely to the PM6's spectrum, some studies show that the measured HOMO can still have contribution from both PM6 and Y6.[47]

The optical absorption spectra for the three samples are shown in Fig. 1b. The Y6 film has an absorption band in the 600 – 900 nm region with the lowest energy peak at ~ 836 nm (1.48 eV), while the PM6 film has an absorption band in the 500 – 700 nm region with the lowest energy peak at ~ 615 nm (2.02 eV). The absorption spectrum of the BHJ film consists of two absorption bands originated from PM6 and Y6. We use the lowest energy peak as the optical band gap for the two materials. These band gaps, together with a small HOMO offset result in a type II band alignment as illustrated in Fig. 1c.

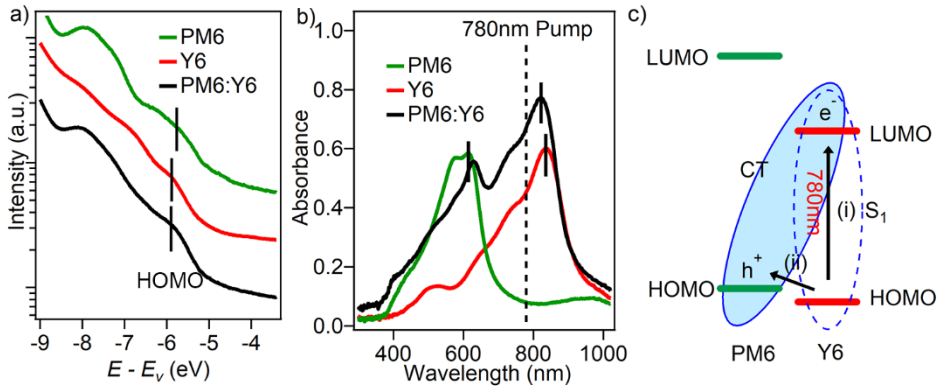

Figure 1: (a) UPS spectra of PM6, Y6, and PM6:Y6 films showing their HOMO peaks. (b) UV-vis absorption spectra of PM6, Y6, and PM6:Y6 films. (c) Schematic diagram showing type II band alignment in the PM6:Y6 BHJ. In our TR-TPPE experiment, electrons in Y6's HOMO are excited to form S_1 excitons by the pump laser pulse (arrow i). Then, holes in Y6 can transfer to PM6 creating CT excitons (arrow ii).

In our TR-TPPE experiment on the PM6:Y6 blend, singlet (S_1) excitons in Y6 are selectively excited by a pump pulse with a photon energy of 1.59 eV (arrow 'i' in Fig. 1c). This photon energy is much smaller than the PM6's band gap. Hence, the pump pulse cannot excite electrons into the PM6's LUMO. Indeed, a control experiment done on the neat PM6 film does not show any pump induced TPPE signal (Fig. S3 in supporting information). Because the pump-induced signal can only originate from Y6, the presence of the pump-induced TPPE signal from the BHJ sample indicates that its surface contains Y6 molecules. Moreover, because of the type II band alignment, only holes in Y6 can be transferred to the PM6 (arrow 'ii' in Fig. 1c). This

experimental design ensures that excited electrons always remain in Y6 domains. Excited electrons in Y6 are photoionized by a time-delayed UV probe pulse with a photon energy of 4.64 eV. The kinetic energy of the ionized electron is measured by the photoelectron spectrometer to obtain the TPPE spectrum. Although ionized electrons always originate from the lowest unoccupied molecular orbital (LUMO) of Y6, the kinetic energy of ionized electrons can be reduced by an amount equal to the exciton binding energy if the electron is bound by a hole. Hence, the TR-TPPE method allows us to resolve the energy difference between CT and CS states.[40, 46, 54] Note that our experiment excites/detects the Y6 domain. To increase the photoemission signal, we used a PM6:Y6 blend with a weight ratio of 1:3 instead of the typical ratio of 1:1.2. Previous works have shown that changing the ratio to 1:3 only slightly lowers the power conversion efficiency.[55, 56]

Figure 2a shows the TR-TPPE spectrum of the PM6:Y6 blend. The background photoemission signal from the negative delay-time is subtracted from the spectrum at each delay time to obtain the pump-induced two photon signal. This pump-induced signal corresponds to photoelectrons originated from excited states. In the TPPE spectrum, the energy of the excited state (the intermediate state energy) is referenced with respect to the HOMO peak position obtained from the same sample, i.e. the E - E_{HOMO} energy scale used in Fig. 2a. Here, we note that the HOMO's peak position instead of the edge position is used for referencing the TPPE spectrum. The technical explanation is provided in Sec. III in the supporting information. Because excited electrons reside in Y6 domains, the energy scale, $E - E_{HOMO}$, can also be written as:

$$(E - E_{HOMO}) = E_{LUMO}^{Y6} - E_{HOMO} - Ex_b, \quad (1)$$

where E_{LUMO}^{Y6}, E_{HOMO}, Ex_b are the Y6's LUMO energy, the average HOMO energy obtained from the UPS spectrum, and the exciton binding energy, respectively.

Near $t = 0$, a peak located at ~ 1.43 eV is observed (the dashed line in Fig. 2a). Because S_1 excitons in Y6 are populated directly by the pump pulse, the position of this peak should be roughly equal to the S_1 energy of Y6. Indeed, this energy is in good agreement with the lowest energy optical absorption peak of the PM6:Y6 blend (~1.51 eV in Fig. 1b). For comparison, the TR-TPPE spectrum of the neat Y6 film is shown in Fig. 2b. A peak at a similar position (~1.48 eV) is observed. This energy is slightly larger than that of the PM6:Y6 blend. For the PM6:Y6 blend, the HOMO peak obtained from the UPS spectrum can have contribution from both the Y6 and PM6. Because the PM6's HOMO is at a slightly higher energy than the Y6's HOMO, E_{HOMO} used in Eq. (1) to calculate the exciton energy is higher than the actual Y6's HOMO. This explains why the S_1 energy appears to be lower in the PM6:Y6 spectrum.

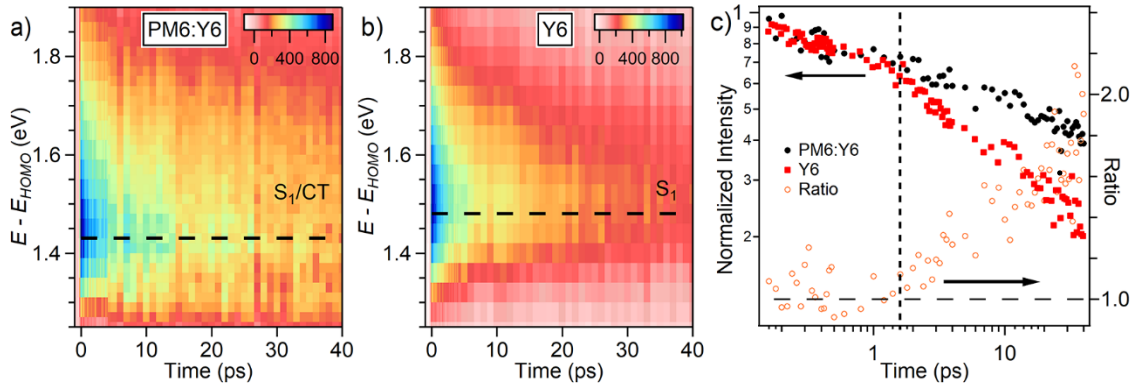

Figure 2: TR-TPPE spectra of (a) the PM6:Y6 blend, and (b) the neat Y6 film for t up to 40 ps. (c) The integrated intensity of the two spectra as a function of time (solid symbols). The two samples have similar decay dynamics in the first 2 ps. However, the two curves diverge for $t > 2$ ps and the PM6:Y6 blend shows a slower decay rate. We attribute the slower intensity decay to the formation of CT excitons in the PM6:Y6 blend. The ratio of the two curves is also plotted (open symbol). This ratio starts to deviate from unity at $t \sim 2$ ps.

Even though the same S_1 peak is observed in the neat Y6 films and the PM6:Y6 blend near $t = 0$, the signal decays differently for the two samples. Figure 2c shows the integrated intensity of the photoemission peak as a function of time. To compare the two curves, the intensity at $t = 0$ is normalized to one. The two decay curves show very similar dynamics up to $t \sim 2$ ps at which they

begin to diverge. For $t > 2$ ps, the signal for the PM6:Y6 blend clearly shows a longer lifetime. We attribute this longer lifetime to the formation of CT excitons in the PM6:Y6 blend, which are expected to have a longer lifetime than Y6's S_1 excitons. The time at which the two curves diverge (~ 2 ps) should correspond to the average hole transfer time from Y6 to PM6. This hole transfer time agrees well with previous ultrafast measurements,[36, 38, 57] which report a hole transfer time in the range of ~ 0.2 – 10 ps in PM6:Y6 BHJs. The transition can be visualized more clearly by taking the ratio of the two decay curves, which is shown as the open circles in Fig. 2c. The ratio begins to deviate from unity at $t \sim 2$ ps.

Note that in our TPPE spectrum (Fig. 2a), we do not notice significant shift in the peak position at $t \sim 2$ ps, which suggests that S_1 and CT excitons have a very similar exciton binding energy. This is because the energy measured in our spectrum (E in Eq. (1)) is equal to $E_{LUMO}^{Y6} - Ex_b$, and the separation of the S_1 and CT peaks in the spectrum is equivalent to the difference in exciton binding energies of S_1 and CT excitons (ΔEx_b^{S1-CT}). The ΔEx_b^{S1-CT} can be expressed as (see Supporting information, Sec. IV):

$$\Delta Ex_b^{S1-CT} = (E_{HOMO}^{PM6} - E_{HOMO}^{Y6}) - (E_{S1}^{Y6} - E_{CT}). \quad (2)$$

In this equation, the $E_{HOMO}^{PM6} - E_{HOMO}^{Y6}$ term represents the HOMO offset between PM6 and Y6. E_{S1}^{Y6} and E_{CT} represents the energy of the Y6 S_1 exciton and the CT exciton, respectively. All energies on the right side of Eq. (2) have been widely reported in the literature. As we mention earlier, we take $E_{HOMO}^{PM6} - E_{HOMO}^{Y6} \sim 0.2$ eV.[52] The difference in the exciton energies, $E_{S1}^{Y6} - E_{CT}$, is typically reported to be ~ 0.1 – 0.2 eV. [14, 15, 52] Hence, the two brackets on the right side of Eq. (2) roughly cancel each other, which gives $\Delta Ex_b^{S1-CT} < 0.1$ eV. The agrees with our TPPE spectrum, which shows a small ΔEx_b^{S1-CT} that cannot be resolved by our setup.

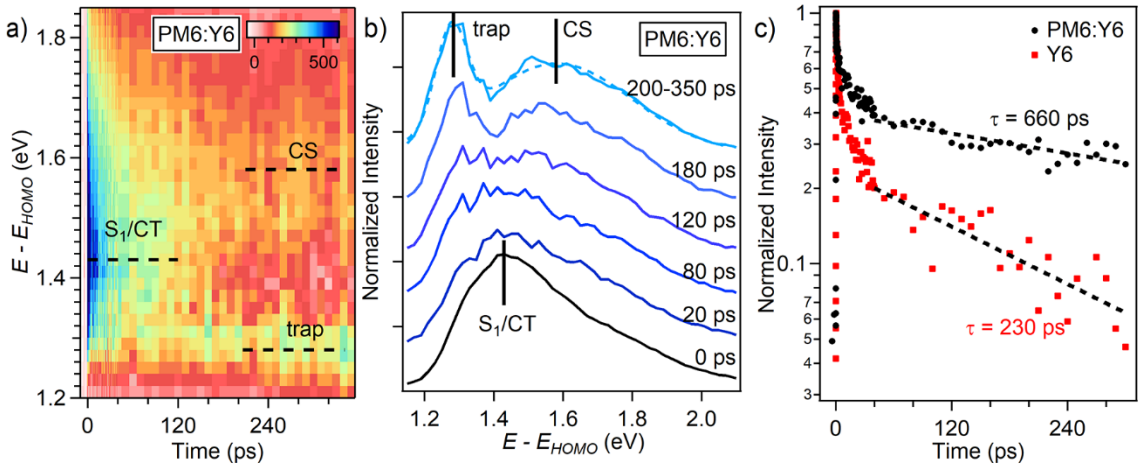

Fig. 3: (a) The TR-TPPE spectrum of the PM6:Y6 blend at longer delay times. The S_1/CT peak bifurcates into a higher energy CS state and a lower energy trap state. (b) The TPPE spectra at various delay times. To compare the spectral shape, we normalize each spectrum with its total area under the curve. The spectra are also offset vertically for clarity. (d) The normalized photoemission intensity as a function of time for the PM6:Y6 blend and the neat Y6 film. The intensity decay for $t > 40$ ps is fitted with an exponential decay (dashed lines). The decay time constants (τ) are indicated on the figure.

Figure 3a shows the TR-TPPE spectrum for the PM6:Y6 blend at longer delay times. Interestingly, the S_1/CT peak bifurcates into two states at $t \sim 100$ ps. We attribute the higher and lower energy states to the CS state and a trap state, respectively. The trap state can be either trapped CT excitons or trapped Y6's S_1 excitons that cannot be converted into CT excitons in the first place. We assign this lower energy state to excitons instead of polarons because they are found to be emissive. As shown in time-resolved photoluminescence (TR-PL) measurement that we will present, this lower energy state has a radiative lifetime similar to that of the exciton in the neat Y6 film. While it is typical that excitons funnel into lower energy sites at longer delay times, the conversion into a higher energy CS state is rather uncommon. Figure 3b shows a series of TPPE spectra at various delay times. All spectra are normalized by their respective total area, so that their spectral shape can be compared. The averaged spectrum from $t = 200 – 350$ ps (the topmost curve) is fitted with two Gaussian functions (the fit is shown as the dashed line). Two peaks centered at ~ 1.58 eV (CS state) and ~ 1.28 eV (trap state) are found. The energy of the CS state is ~ 0.15 eV

higher than the energy of the CT state. This energy difference can be attributed to the exciton binding energy of the CT exciton. We note that previous works have shown that the minimum separation between electron and hole in a localized CT exciton is ~ 22 Å.[27] By using a generic dielectric constant of ~ 4, we can obtain a Coulomb potential energy of 0.16 eV, which agrees reasonably well with the observed CT exciton binding energy. Hence, our data suggests that the localized CT state, which is generated initially at the interface, dissociates into a free electron-hole pair spontaneously within ~ 100 ps (probably *via* some delocalized CT states). Although similar CS times (10 – 100 ps) have been reported in previous works,[19, 38, 39] our measurement provides direct evidence that the CS process is an enthalpy uphill process.

The observation of an enthalpy uphill process is notable because our samples are not attached to any external electrodes for charge extraction. On the 1 – 100 ps timescale, excited electrons typically equilibrate with the environment by relaxing into lower energy states. By the principle of detailed balance, if the enthalpy change (ΔE) is the only contribution to the free energy change (ΔF), the ratio of the concentration of the higher enthalpy CS state to that of the lower enthalpy localized CT state should be given by $\exp(-\Delta E/k_B T)$, in which k_B and T are the Boltzmann constant and the temperature, respectively. In our case, ΔE ~0.15 eV, which results in a ratio of ~ 2.5×10^{-3}, i.e., the equilibrium concentration of the CS state should be ~ 3 orders of magnitude smaller than the localized CT state. This low concentration should make the higher energy CS state unobservable in our spectrum. Instead, our spectrum shows a spectral shift towards higher energies at longer delay times. Hence, terms other than ΔE must contribute significantly to ΔF. Because our film is not subjected to any external field that would have lowered the free energy of the CS state, we conclude that the entropic driving force ($-T\Delta S$) should have a significant contribution to the free energy change ($\Delta F = \Delta E - T\Delta S$) in the CS process. If the $-T\Delta S$ can compensate ΔE, the

CS process is essentially barrierless (in terms of free energy). This is consistent with a previous experimental observation that the energy barrier for charge generation appears to be zero near room temperature, but the barrier increases at lower temperatures.[39, 41] The barrier increase at lower temperatures can be explained by the diminishing of the entropy driving force ($T\Delta S$).

Indeed, the measurement made at the low temperature (~170 K) does not show a clear CS peak (Fig. S4, supporting information), which suggests a decrease in the equilibrium population of the free carrier relative to that of the exciton. This observation agrees with the weakening of the entropy driving force. However, a small free carrier population may still exist at 170 K. In the spectrum shown in Fig. S4, the high energy side of the exciton peak extends up to ~ 2.0 eV. In Fig. 3b, the CS peak is at ~ 1.6 eV. Therefore, the signal from the CS state can be hidden in the high energy tail of the exciton peak if the concentration of the free carrier is low. For instance, previous transient absorption spectroscopy work shows that the CS process is slower and has a smaller yield at 180 K as compared to that at the room temperature.[39] A low yield at low temperatures would make the CS peak indistinguishable from the main exciton peak in our TPPE spectrum.

In our experiment on the PM6:Y6 film, a significant population of trapped excitons is found in our spectrum (Fig. 3a), which seems to contradict the near-unity internal quantum efficiency of PM6:Y6 OPVs. However, in our spectroscopy measurement, the active layer does not contain any internal electric field induced by electrodes. Essentially, our active layer is in an open-circuit condition. Therefore, an equilibrium mixture of separated carriers and trapped excitons is produced. On the other hand, in an operating OPV device, separated carriers are removed continuously from the active layer. When free carriers are removed, they can be repopulated from excitons to reestablish the equilibrium, which can lead to a much higher CS yield. The presence of

an internal field in a device would also further reduce the energy barrier for CS, which can account for the high quantum efficiency even at temperatures as low as ~ 100 K.[41]

The same experiment was also performed on the neat Y6 film, and we do not observe any spectral shift other than a monotonic decay of the exciton population (see supporting information, Fig. S5). Therefore, our results suggest that higher-enthalpy free carriers cannot be formed spontaneously in neat Y6 films. We note that some recent works have suggested that free carriers can be generated from intra-moiety excitons (i-EX) in Y6 domains.[37, 38, 58] The i-EX is akin to a S_1 exciton with a CT character, in which its electron and hole reside at different parts of the Y6 molecule. The i-EX can be formed in Y6 domains immediately (~ 100 fs) after photoexcitation, which can then be separated into free carriers in a PM6:Y6 BHJ film in ~15 ps.[38] Compared to our current work, we think that the S_1/CT peak in our TPPE spectrum, which is observed on a similar timescale (100 fs – 10 ps), can be contributed by the i-EX as well. Previous works have not shown whether the i-EX is bound or not. In the light of our present work, we argue that the i-EX is bound and has a similar exciton binding energy as the S_1/CT state. Because we do not observe any enthalpy-uphill CS process occurring in the neat Y6 film, the i-EX is likely to separate at the PM6:Y6 interface after a hole transfer process. The need for D/A interfaces to generate free carriers is also consistent with the poor performance of OPVs consisting of a neat Y6 film as the active layer when the donor polymer is absent.[35, 37, 56]

Finally, we compare the signal decay dynamics between neat Y6 and PM6:Y6 films. For this purpose, the photoemission intensity is integrated across the whole spectral range to include all states with different energies. Figure 3c shows the temporal evolution of this integrated intensity, with the intensity at $t = 0$ normalized to one. We note that the signal decays faster at $t <$ 40 ps. However, these earlier decays can originate from factors other than the population decay.

Processes such as hot exciton relaxation,[59, 60] and the conversion between different excited states (S_1, CT, and CS states) can change the measured photoemission signal as well because different excited states can have different photoionization cross-sections. However, for longer times, when the excitation no longer converts between different species, the signal intensity should correlate with the population. In both samples, the signal decays exponentially at $t > 40$ ps. The observed decay time constants for PM6:Y6 and neat Y6 films are 660 ps, and 230 ps respectively. The longer lifetime observed in PM6:Y6 is consistent with the generation of free carriers in the PM6:Y6 film, which should have a much longer lifetime compared to the exciton.

We have also conducted time-resolved photoluminescence (TR-PL) measurements on the PM6:Y6 and the neat Y6. The PL signal mainly originates from the Y6's S_1, although the CT exciton can also couple strongly with (and emit through) the Y6's S_1.[12] Our TR-PL data is shown in Fig. S6 (supporting information). The neat Y6 film shows an exciton lifetime of ~ 420 ps, which is somewhat larger than the lifetime measured by the TPPE (~ 230 ps). Because TPPE is a surface sensitive technique, the result indicates that the surface population decays faster than the bulk population. We note that immediately after the photoexcitation, the exciton population falls exponentially with the distance from the surface. Diffusion of excitons from the surface to the bulk can lead to a faster population decay at the surface, which can explain its shorter lifetime. Interestingly, for the PM6:Y6, half of the signal decays at a faster time constant of ~ 110 ps, which corresponds to the time when the enthalpy-uphill CS is observed (Fig. 3a). This result confirms our assignment of the higher energy state in the TPPE spectrum to the CS state because separated carriers can no longer recombine radiatively, which leads to the quenching of the PL signal. The other half of the population decays at a slower lifetime (~390 ps) that is close to the lifetime found

in the neat Y6 film. This slower decay component can be assigned to trapped excitons (the lower energy state in Fig. 3a).

After showing that the enthalpy-uphill CS, likely to be driven by entropy, can occur in the PM6:Y6 blend, we proceed to another important question on what kind of morphology would enhance the entropic driving force. To this end, we have done structural characterizations on our PM6:Y6 blend. Figure 4a shows the grazing incidence wide angle X-ray scattering (GIWAXS) pattern of the PM6:Y6 blend. GIWAXS patterns for other controlled samples, such as neat Y6, neat PM6 and PEDOT:PSS films, are provided in the supporting information (Fig. S7). The GIWAXS pattern shows a board, isotropic diffraction ring at a wavevector (q) ~ 1.56 $Å^{-1}$, which can be observed when either the PM6 polymer or the PEDOT:PSS layer is present (Fig. S7). We assign this diffraction ring to the π-π stacking peak of the polymer film. The scattering intensity along the out-of-plane (vertical) and in-plane (horizontal) directions of the GIWAXS pattern of the PM6:Y6 blend are shown in Fig. 4b. In addition to the peak related to the diffraction ring (green line), another peak at q ~ 1.78 $Å^{-1}$ (3.53 Å) can be observed in the out-of-plane direction (red line). This peak is observed only when Y6 is present. Hence, we assign this peak to the π-π stacking peak of Y6. This assignment is consistent with previous works.[2, 27] The 1.78 $Å^{-1}$ peak only appears in the out-of-plane direction, which implies that Y6 molecules have a face-on orientation.

To measure the periodicity at smaller q (longer length scales), we employed the grazing incidence small angle X-ray scattering (GISAXS). The GISAXS pattern for the PM6:Y6 blend is shown in Fig. 4c, and GISAXS patterns for other controlled samples can be found in Fig. S8 in the supporting information. In the GISAXS pattern, an intense stripe can be found along the out-of-plane direction, which can be originated from the surface roughness. We will focus on the intensity cut along the in-plane direction, which shows clearer diffraction peaks. In the line cut along the in-

plane direction (Fig. 4d), a peak at ~0.29 $Å^{-1}$ (*d*-spacing of 21.7 Å) and a shoulder at ~ 0.40 $Å^{-1}$ (*d*-spacing of 15.7 Å) can be found for the PM6:Y6 blend. The peak at ~0.29 $Å^{-1}$ can be contributed from both PM6 and Y6 because it can be found in both PM6 and Y6 neat films. However, the shoulder at ~ 0.4 $Å^{-1}$ is unique to Y6. Previous work has assigned this peak to the lamellar diffraction peak of Y6 which corresponds to the distance of the end group between two neighboring Y6 stacks.[27] The appearance of the lamellar peak in the in-plane direction further confirms that Y6 molecules have a face-on orientation. We also plot the scattering intensity in the in-plane direction for very small q (Fig. 4e). On top of the monotonically decaying background, intensity bumps at different locations for different samples can be found (labelled by arrows). These linecuts can be fitted to obtain the PM6 and/or Y6 domain sizes (see supporting information, Fig. S9). The domain sizes obtained from the fit for the PM6:Y6, neat PM6, and neat Y6 films are 52 nm, 19 nm, and 113 nm, respectively. As we will show, very similar domain sizes can also be found from atomic force microscopy (AFM) images.

Figure 4f and g show the topology and phase images of the PM6:Y6 blend measured by AFM. While the topology image provides information such as the surface roughness, the phase image can reveal features like grain and domain boundaries. In the phase image shown in Fig. 4g, some fine, elongated features are observed which can be attributed to the nano-fibrous structure of the polymer network. [5, 6, 10, 55] Intertwined fiber-like domains are even more clear in the phase image of the neat PM6 film (Fig. S10 in the supporting information). To determine the characteristic domain size of the structure, we calculate the radial power spectral density (r-PSD), i.e., the Fourier transform of the autocorrelation function, of the phase image. The r-PSD curves are shown in Fig. 4h. The peak positions of the r-PSD curves are found by fitting the peak with a Gaussian function. Domain sizes determined from the peak position are 40 nm (PM6:Y6), 23 nm

(neat PM6), and 112 nm (neat Y6), which agrees well with those determined by GISAXS (52 nm for PM6:Y6, 19 nm for PM6, and 113 nm for Y6). The neat PM6 film shows a polymer network with the smallest periodicity of ~20 nm. For the PM6/Y6 blend, the contrast in the phase image is mainly contributed by the polymer network,[5, 6, 10, 55] and the characteristic size is increased to ~40 – 50 nm. The polymer network appears to be enlarged as Y6 domains are incorporated into the polymer network. Finally, the phase image of the neat Y6 film does not show elongated fiber-like domains, and the ~100 nm length scale should correspond to the average grain size of the Y6 film.

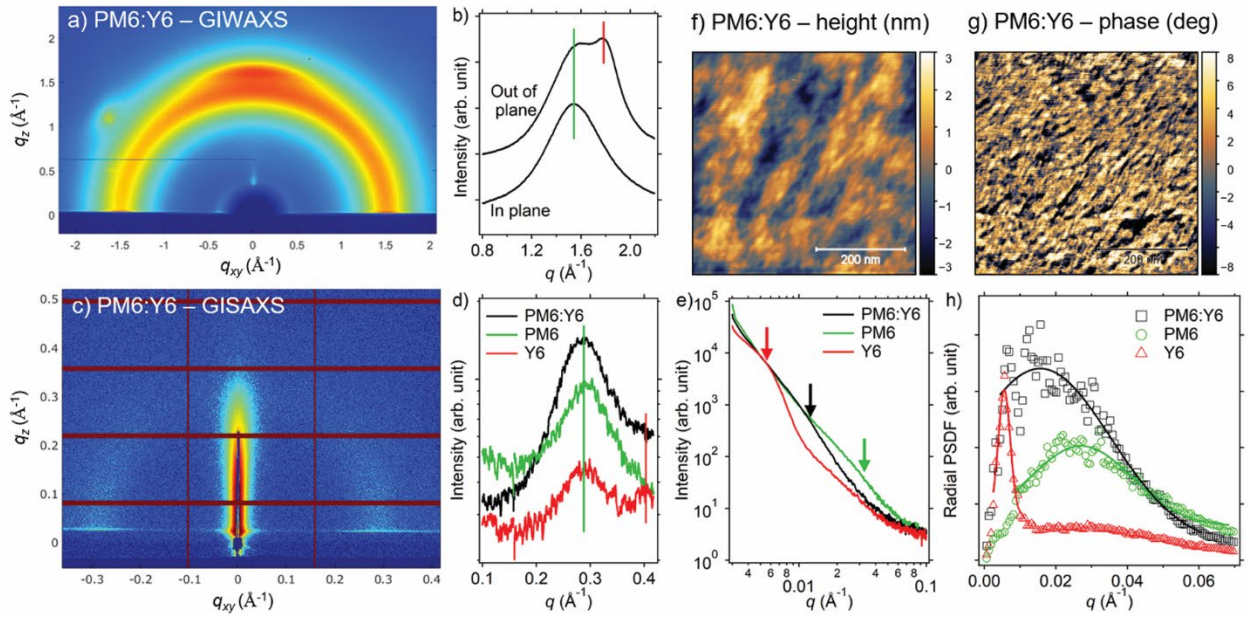

Figure 4: (a) The GIWAXS pattern for the PM6:Y6 blend. (b) The intensity cut for the pattern shown in (a) along the out-of-plane and in-plane directions. (c) The GISAXS pattern of the PM6:Y6 blend. (d, e) The intensity cut along the in-plane direction of GISAXS patterns of PM6:Y6, neat PM6, and neat Y6 films. (f) The AFM topology, and (g) phase images of the PM6:Y6 film. (h) Radial PSD functions calculated from phases images of PM6:Y6, neat PM6, and neat Y6 films.

The X-ray scattering and AFM images capture two important characteristics of the PM6:Y6 BHJ film. First, planar Y6 molecules stack in the direction perpendicular to the surface (captured by GIWAXS), and probably form some rod-like domains along the same direction due to the strong π-π coupling in this direction. Second, the PM6 forms nano-sizes bundles which intertwine with

each other to form a mesh-like structure in which the polymer chain lays parallel to the substrate (captured by AFM) and the π-π stacking direction between polymer chains is either parallel or perpendicular to the surface (captured by GIWAXS). The two structural features are summarized schematically in Fig. 5a. In this figure, each domain consists of multiple stacks of Y6 molecules or multiple polymer chains. We note that the electron in the CT exciton primarily delocalizes along the π-stacking direction in the Y6 stack and the hole primarily delocalizes along the PM6-polymer chain. To illustrate how the CT exciton would look like, in Fig. 5b, we only draw a stack of Y6 molecules and a PM6 polymer chain that touches each other. Because the polymer chain and the Y6-stack are oriented in different directions, CT excitons are likely to form at intersection points where the two domains met. At these intersections, the delocalized electron and hole in a CT exciton should primarily be in contact with each other through a point-like junction (Fig. 5b) based on their relative orientation, which has a minimal contact area. The contact area between electron and hole wavefunctions can further be reduced by bulky and irregular side-groups of the Y6 and PM6, which tends to isolate the core of the Y6 from that of the PM6.

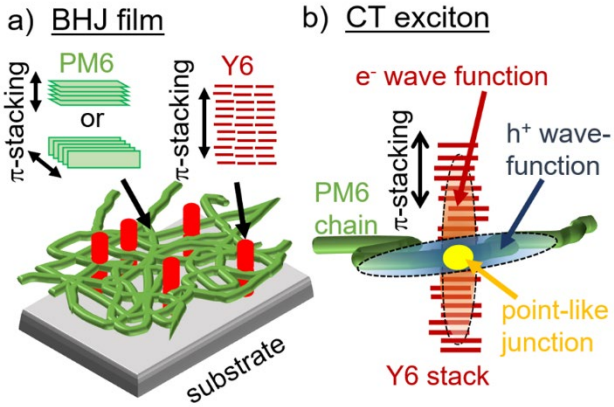

Figure 5: Schematic diagrams showing (a) the morphology of the PM6:Y6 film, and (b) the delocalized electron and hole wavefunctions within the CT exciton. In (a), each domain consists of multiple stacks of Y6 molecules or multiple polymer chains. The morphology of the PM6:Y6 allows the electron and hole wavefunctions within the CT exciton to form a point-like junction, which can maximize the entropic driving force.

Previously, we have investigated the CS dynamics in several model D/A interfaces with various molecular orientations, and with fullerene and non-fullerene-planar electron acceptors.[40, 45, 46, 61, 62] We found that the enthalpy-uphill CS occurs only at interfaces where the delocalized electron and hole form point-like junctions.[45, 46, 61] For other interfaces, the more conventional hot CT-exciton cooling is observed.[26, 40, 45, 62] By modeling the density of CT/CS states at different interfaces as a function of the energy,[45, 46] we found that a point-like contact can suppress the density of localized CT states relative to the density of delocalized ones. Hence, the density of state for CT/CS states can increase more rapidly with the energy, which can increase the entropic driving force. Likewise, in the case of PM6:Y6, the combination of morphology and anisotropic electron delocalization restricts the delocalized electron and hole to contact *via* isolated point-like junctions. This structural feature can promote spontaneous enthalpy uphill CS because it enlarges the entropic driving force.

The key requirement for enabling the entropy-driven CS is that delocalized electron and hole form a point-like junction within a CT exciton. We argue that these point-like junctions can be generally found in other high-performance Y-series NFAs/polymer BHJs beyond PM6:Y6. Specifically, the following structural characteristics commonly found in these BHJs can result in the point-like junction as shown in Fig. 5b. First, most Y-series NFAs form anisotropic domains with the π-stacking direction orienting along the substrate's normal direction. This is orthogonal to polymer domains, which typically lie parallel to the substrate. Second, Y-series NFAs and donor polymers typically have some peripheral groups that are irregular in shape. These irregular side groups can prohibit the core moiety of the NFA and polymer, at which the electron and hole wavefunctions are located, from forming a large spatial contact with each other. Third, in many Y-series NFA/polymer BHJs, both donor and acceptor domains have a good crystallinity, which can

enable extensive electron/hole delocalization within individual domains. Delocalization is essential for achieving a high density of loosely bound CT and CS states. Here, we argue that materials and devices that can take advantage of the entropy-driven CS mechanism should have the above three structural characteristics. For example, a recent work on high-performance all-small-molecules NFA OPVs contains donor and acceptor molecules that are stacked in orthogonal directions.[63] Another recent works on NFA/polymer OPVs shows nano-fibril-like domains of polymers and NFAs do not lie parallel with respect to each other, but they intersect rather randomly with each other through point-like junctions.[10] These are sample structures that can favor the entropy-driven CS.

Finally, we note that while entropic driving force is often discussed in terms of its role in facilitating CS, it could reduce the recombination rate as well. This is because the entropic driving force, if it is large enough ($T\Delta S > \Delta E$), can become a barrier for the reverse of the CS process – the recombination of electron-hole pairs back to CT excitons. Because a CT exciton is a precursor for the electron-hole recombination, a large enough entropic driving force can suppress the bimolecular recombination rate and increase the carrier lifetime. This can explain the long carrier lifetime often observed in NFA BHJs.[9, 19, 36] An increased carrier lifetime can in turn reduce the recombination loss in the open circuit voltage and improve the overall power conversion efficiency.

3. Conclusion

In conclusion, we have shown that the CS process in PM6:Y6 BHJs is an endothermic process with an enthalpy barrier of ~0.15 eV. The CS can occur spontaneously within 100 ps without any external field despite it is an enthalpy-uphill process. This observation is in contrast with many proposed CS mechanisms, which are based on arguments that either the enthalpy barrier

is absent, or charges are extracted from CT excitons by sites with lower potential energies. Our result shows that an enthalpy barrier is indeed present, but it would be overcome spontaneously by the entropy driving force. We further propose that the entropy driving force is enhanced in NFA/polymer BHJs because its morphology and structural anisotropy are likely to prohibit delocalized electron and hole wavefunctions within the CT excitons to form an extensive spatial contact. Hence, a major portion of CT excitons are likely to have its electron and hole wavefunctions in contact with each other through point-like junctions, which can significantly reduce the density of localized CT states relative to delocalized ones and enhance the entropic driving force. An entropy-driven CS is intrinsically an energy gain process as it allows a CT exciton to gain energy from the thermal bath. Therefore, it can uniquely account for the very low energy loss observed in recent NFA OPVs.

4. Experimental Section

Sample preparation – Reagents and chemicals were purchased directly from commercial vendors. PM6 and Y6 were obtained from Solarmer Energy, Inc. For optical absorption, AFM, UPS, and TR-TPPE measurements, the organic films were fabricated on PEDOT:PSS/ITO/glass. Initially, ITO/glass substrates were subjected to ultrasonic cleaning using detergent, DI water, acetone, and IPA for a duration of 15 minutes each. After the cleaning process, substrates were dried with N_2 gas. Then, they were placed in an oven at 80°C for 20 minutes for further drying. Finally, ITO/glass substrates were treated by O_2 plasma for 10 minutes, before transferring to a N_2-glove box for spin-coating. PEDOT:PSS (Sigma-Aldrich, conductive grade, 483095) was spin-coated onto the substrates at a speed of 4000 rpm for 1 minute. The coated substrates were then baked on a hot plate at 150°C for 20 minutes. The PM6:Y6 blend solution was prepared in chloroform with a mixing weight ratio of 1:3. The total concentration was kept at 16 mg/mL.

Similarly, for neat PM6 and neat Y6 films, the solution was prepared in chloroform with a concentration of 8 mg/mL. Solutions were stirred at 40°C for 3 hours before being spin-coated onto the PEDOT: PSS layer at a speed of 2500 rpm for 40 seconds. Finally, samples were annealed at 110°C for 10 minutes, completing the fabrication process.

UPS experiments – All photoemission spectroscopy experiments were done in an ultra-high vacuum (UHV) chamber with a base pressure of ~1×10^{-10} Torr. A standard UV lamp was used to generate UV light for the UPS measurement. The He-I emission line, which has a photon energy of 21.22 eV, was used in our experiment. The energy and emission angle of the photoelectrons were measured using a hemispherical analyzer equipped with an imaging detector (Phoibos 100, SPECS).

TR-TPPE experiment – The energy and population of the excited states were measured using a pump-probe approach. The pump beam had a photon energy of 1.59 eV, while the time-delayed probe beam had a photon energy of 4.64 eV. The pump and probe beams were generated from the outputs of two noncollinear optical parametric amplifiers (NOPAs), Light Conversion Orpheus-N-2H and -N-3H, which were pumped by a Yb:KGW regenerative amplifier running at 125 kHz (Light Conversion Pharos 10 W). The pump and probe pulses had pulse durations of 25 and 65 fs, respectively. The full width at half maximum (fwhm) of the Gaussian profile (pulse energy) of the pump and probe pulses at the sample were 1.0 mm (132 nJ) and 0.85 mm (2 nJ), respectively. At an incidence angle of 30º, the peak fluence at the center of the pump beam is 10.12 μJ cm^{-2}. We estimate that an initial excitation density of 6.2×10^{18} cm^{-3} is produced by a pump pulse by using the optical constants reported in Ref. [64] (see supporting information, Sec. VIII). The kinetic energy of the emitted photoelectrons was measured using a hemispherical electron analyzer equipped with an imaging detector (Phoibos 100, SPECS).

TR-PL experiment – In this experiment, the sample was excited by 25 fs laser pulses with a central wavelength of 660 nm. These pulses were generated by the same laser system described above. The pump fluence at the sample is ~5.43 μJ cm^{-2}. The time-resolved data was collected by a time-correlated single photon counter (PicoQuant, PicoHarp 330). A pair of low/high pass 750-nm filters was used to block the pump laser light from entering the single photon counter. The frequency-resolved spectrum was collected by an interferometer setup (NIREOS, Gemini Interferometer).

GIWAXS/GISAXS measurement – The grazing incidence small-angle and wide-angle x-ray scattering measurements were performed at Beamline 12-ID-B of the Advanced Photon Source (APS) at Argonne National Laboratory (Lemont, IL). An Eiger2 9M detector (DECTRIS) was used for GISAXS measurements and the sample-to-detector distance was set 2.0 meters. The GIWAXS data were collected using a Perkin Elmer XRpad detector with the sample-to-detector distance of ca. 180 mm. The X-ray energy was 13.3 keV for both GISAXS and GIWAXS measurements. The linecuts were done using the beamline software. To avoid the diffraction peaks originated from the ITO substrate, the samples used for X-ray measurements were fabricated SiO_2 (300 nm)/Si wafer instead of ITO/glass using the same procedure outlined above.

AFM measurement and analysis – AFM measurements were obtained using a Digital Instruments Multimode Nanoscope IIIA instrument. Tapping mode images were collected using NSC35 probe tips (NanoAndMore) with a resonance frequency of ~150 kHz with a 1 Hz scan rate. Images were collected at 3-5 locations on each sample at multiple different scan sizes ranging from 500 nm to 5 μm. The r-PSD functions are calculated by the open-source program Gwyddion (http://gwyddion.net/). The average of the r-PSD functions calculated from three 1 μm × 1 μm images collected from different areas was used.

Statistical analysis – The raw TR-TPPE spectrum contains background signal originates from the probe pulse (not the pump-induced signal). The spectrum collected at negative delay times was treated as the background signal and it was subtracted from each time-delayed spectrum to obtain the pump-induced signal. For each data set, we collected 3- 5 independent spectra from different areas of the samples. Those spectra were averaged to obtain the final spectrum. For the TR-PL data, the frequency-resolved spectra were obtained from the Fourier transform of the interferogram using the software provided by the manufacturer of our interferometer.

Acknowledgement:

This material is based upon work supported by the U.S. Department of Energy, Office of Science, Office of Basic Energy Sciences, Chemical Sciences, Geosciences, and Biosciences Division under Award Number DE-SC0024525. W. L. C. also acknowledges the support from the University of Kansas General Research Fund allocation #2151080. C. L. B. was supported by the National Science Foundation under award CHE-2108448 as well as the University of Kansas General Research Fund # 2112080. F.R. acknowledges the scholarship support from Jazan University. This research used the beamline 12-ID-B of the Advanced Photon Source, a U.S. Department of Energy (DOE) Office of Science user facility at Argonne National Laboratory and is based on research supported by the U.S. DOE Office of Science-Basic Energy Sciences, under Contract No. DE-AC02-06CH11357. H.-L. Y acknowledges the support from the University Grants Committee of Hong Kong (GRF 11307323).

References:

(1) Scharber, M. C.; Sariciftci, N. S. Efficiency of bulk-heterojunction organic solar cells. *Prog. Polym. Sci.* **2013**, *38*, 1929-1940.

(2) Yuan, J.; Zhang, Y. Q.; Zhou, L. Y.; Zhang, G. C.; Yip, H. L.; Lau, T. K.; Lu, X. H.; Zhu, C.; Peng, H. J.; Johnson, P. A.; Leclerc, M.; Cao, Y.; Ulanski, J.; Li, Y. F.; Zou, Y. P. Single-Junction Organic Solar Cell with over 15% Efficiency Using Fused-Ring Acceptor with Electron-Deficient Core. *Joule* **2019**, *3*, 1140-1151.

(3) Lin, F.; Jiang, K.; Kaminsky, W.; Zhu, Z. L.; Jen, A. K. Y. A Non-fullerene Acceptor with Enhanced Intermolecular pi-Core Interaction for High-Performance Organic Solar Cells. *J. Am. Chem. Soc.* **2020**, *142*, 15246-15251.

(4) Lin, Y. B.; Firdaus, Y.; Isikgor, F. H.; Nugraha, M. I.; Yengel, E.; Harrison, G. T.; Hallani, R.; El-Labban, A.; Faber, H.; Ma, C.; Zheng, X. P.; Subbiah, A.; Howells, C. T.; Bakr, O. M.; McCulloch, I.; De Wolf, S.; Tsetseris, L.; Anthopoulos, T. D. Self-Assembled Monolayer Enables Hole Transport Layer-Free Organic Solar Cells with 18% Efficiency and Improved Operational Stability. *ACS Energy Lett.* **2020**, *5*, 2935-2944.

(5) Liu, Q. S.; Jiang, Y. F.; Jin, K.; Qin, J. Q.; Xu, J. G.; Li, W. T.; Xiong, J.; Liu, J. F.; Xiao, Z.; Sun, K.; Yang, S. F.; Zhang, X. T.; Ding, L. M. 18% Efficiency organic solar cells. *Sci. Bull.* **2020**, *65*, 272-275.
(6) Cui, Y.; Yao, H.; Zhang, J.; Xian, K.; Zhang, T.; Hong, L.; Wang, Y.; Xu, Y.; Ma, K.; An, C.; He, C.; Wei, Z.; Gao, F.; Hou, J. Single-Junction Organic Photovoltaic Cells with Approaching 18% Efficiency. *Adv. Mater.* **2020**, *32*, 1908205.
(7) Li, C.; Zhou, J. D.; Song, J. L.; Xu, J. Q.; Zhang, H. T.; Zhang, X. N.; Guo, J.; Zhu, L.; Wei, D. H.; Han, G. C.; Min, J.; Zhang, Y.; Xie, Z. Q.; Yi, Y. P.; Yan, H.; Gao, F.; Liu, F.; Sun, Y. M. Non-fullerene acceptors with branched side chains and improved molecular packing to exceed 18% efficiency in organic solar cells. *Nat. Energy* **2021**, *6*, 605-613.
(8) Meng, H. F.; Liao, C. T.; Deng, M.; Xu, X. P.; Yu, L. Y.; Peng, Q. 18.77 % Efficiency Organic Solar Cells Promoted by Aqueous Solution Processed Cobalt(II) Acetate Hole Transporting Layer. *Angew Chem. Int. Ed.* **2021**, *60*, 22554-22561.
(9) Jiang, K.; Zhang, J.; Zhong, C.; Lin, F. R.; Qi, F.; Li, Q.; Peng, Z. X.; Kaminsky, W.; Jang, S. H.; Yu, J. W.; Deng, X.; Hu, H. W.; Shen, D.; Gao, F.; Ade, H.; Xiao, M.; Zhang, C. F.; Jen, A. K. Y. Suppressed recombination loss in organic photovoltaics adopting a planar-mixed heterojunction architecture. *Nat. Energy* **2022**, *7*, 1076-1086.
(10) Zhu, L.; Zhang, M.; Xu, J. Q.; Li, C.; Yan, J.; Zhou, G. Q.; Zhong, W. K.; Hao, T. Y.; Song, J. L.; Xue, X. N.; Zhou, Z. C.; Zeng, R.; Zhu, H. M.; Chen, C. C.; MacKenzie, R. C. I.; Zou, Y. C.; Nelson, J.; Zhang, Y. M.; Sun, Y. M.; Liu, F. Single-junction organic solar cells with over 19% efficiency enabled by a refined double-fibril network morphology. *Nat. Mater.* **2022**, *21*, 656-663.
(11) Zhang, M.; Zhu, L.; Zhou, G. Q.; Hao, T. Y.; Qiu, C. Q.; Zhao, Z.; Hu, Q.; Larson, B. W.; Zhu, H. M.; Ma, Z. F.; Tang, Z.; Feng, W.; Zhang, Y. M.; Russell, T. P.; Liu, F. Single-layered organic photovoltaics with double cascading charge transport pathways: 18% efficiencies. *Nat. Commun.* **2021**, *12*, 309.
(12) Qian, D. P.; Zheng, Z. L.; Yao, H. F.; Tress, W.; Hopper, T. R.; Chen, S. L.; Li, S. S.; Liu, J.; Chen, S. S.; Zhang, J. B.; Liu, X. K.; Gao, B. W.; Ouyang, L. Q.; Jin, Y. Z.; Pozina, G.; Buyanova, I. A.; Chen, W. M.; Inganas, O.; Coropceanu, V.; Bredas, J. L.; Yan, H.; Hou, J. H.; Zhang, F. L.; Bakulin, A. A.; Gao, F. Design rules for minimizing voltage losses in high-efficiency organic solar cells. *Nat. Mater.* **2018**, *17*, 703-709.
(13) Chen, S. S.; Wang, Y. M.; Zhang, L.; Zhao, J. B.; Chen, Y. Z.; Zhu, D. L.; Yao, H. T.; Zhang, G. Y.; Ma, W.; Friend, R. H.; Chow, P. C. Y.; Gao, F.; Yan, H. Efficient Nonfullerene Organic Solar Cells with Small Driving Forces for Both Hole and Electron Transfer. *Adv. Mater.* **2018**, *30*, 1804215.
(14) Karki, A.; Vollbrecht, J.; Dixon, A. L.; Schopp, N.; Schrock, M.; Reddy, G. N. M.; Nguyen, T. Q. Understanding the High Performance of over 15% Efficiency in Single-Junction Bulk Heterojunction Organic Solar Cells. *Adv. Mater.* **2019**, *31*, 1903868.
(15) Wan, P.; Chen, X. T.; Liu, Q.; Mahadevan, S.; Guo, M. X.; Qiu, J. J.; Sun, X. J.; Tsang, S. W.; Zhang, M. J.; Li, Y. F.; Chen, S. Direct Observation of the Charge Transfer States from a Non-Fullerene Organic Solar Cell with a Small Driving Force. *J. Phys. Chem. Lett.* **2021**, *12*, 10595-10602.
(16) Coffey, D. C.; Larson, B. W.; Hains, A. W.; Whitaker, J. B.; Kopidakis, N.; Boltalina, O. V.; Strauss, S. H.; Rumbles, G. An Optimal Driving Force for Converting Excitons into Free Carriers in Excitonic Solar Cells. *J. Phys. Chem. C* **2012**, *116*, 8916-8923.
(17) Liu, X.; Li, Y. X.; Ding, K.; Forrest, S. Energy Loss in Organic Photovoltaics: Nonfullerene Versus Fullerene Acceptors. *Phys. Rev. Appl.* **2019**, *11*, 024060.

(18) Azzouzi, M.; Yan, J.; Kirchartz, T.; Liu, K. K.; Wang, J. L.; Wu, H. B.; Nelson, J. Nonradiative Energy Losses in Bulk-Heterojunction Organic Photovoltaics. *Phys. Rev. X* **2018**, *8*, 031055.
(19) Hinrichsen, T. F.; Chan, C. C. S.; Ma, C.; Palecek, D.; Gillett, A.; Chen, S. S.; Zou, X. H.; Zhang, G. C.; Yip, H. L.; Wong, K. S.; Friend, R. H.; Yan, H.; Rao, A.; Chow, P. C. Y. Long-lived and disorder-free charge transfer states enable endothermic charge separation in efficient non-fullerene organic solar cells. *Nat. Commun.* **2020**, *11*, 5617.
(20) Gillett, A. J.; Privitera, A.; Dilmurat, R.; Karki, A.; Qian, D. P.; Pershin, A.; Londi, G.; Myers, W. K.; Lee, J.; Yuan, J.; Ko, S. J.; Riede, M. K.; Gao, F.; Bazan, G. C.; Rao, A.; Nguyen, T. Q.; Beljonne, D.; Friend, R. H. The role of charge recombination to triplet excitons in organic solar cells. *Nature* **2021**, *597*, 666-671.
(21) Bredas, J. L.; Norton, J. E.; Cornil, J.; Coropceanu, V. Molecular Understanding of Organic Solar Cells: The Challenges. *Acc. Chem. Res.* **2009**, *42*, 1691-1699.
(22) Clarke, T. M.; Durrant, J. R. Charge Photogeneration in Organic Solar Cells. *Chem. Rev.* **2010**, *110*, 6736-6767.
(23) Ostroverkhova, O. Organic Optoelectronic Materials: Mechanisms and Applications. *Chem. Rev.* **2016**, *116*, 13279-13412.
(24) Savoie, B. M.; Jackson, N. E.; Chen, L. X.; Marks, T. J.; Ratner, M. A. Mesoscopic Features of Charge Generation in Organic Semiconductors. *Acc. Chem. Res.* **2014**, *47*, 3385-3394.
(25) Gelinas, S.; Rao, A.; Kumar, A.; Smith, S. L.; Chin, A. W.; Clark, J.; van der Poll, T. S.; Bazan, G. C.; Friend, R. H. Ultrafast Long-Range Charge Separation in Organic Semiconductor Photovoltaic Diodes. *Science* **2014**, *343*, 512-516.
(26) Jailaubekov, A. E.; Willard, A. P.; Tritsch, J. R.; Chan, W. L.; Sai, N.; Gearba, R.; Kaake, L. G.; Williams, K. J.; Leung, K.; Rossky, P. J.; Zhu, X. Y. Hot charge-transfer excitons set the time limit for charge separation at donor/acceptor interfaces in organic photovoltaics. *Nat. Mater.* **2013**, *12*, 66-73.
(27) Zhang, G. C.; Chen, X. K.; Xiao, J. Y.; Chow, P. C. Y.; Ren, M. R.; Kupgan, G.; Jiao, X. C.; Chan, C. C. S.; Du, X. Y.; Xia, R. X.; Chen, Z. M.; Yuan, J.; Zhang, Y. Q.; Zhang, S. F.; Liu, Y. D.; Zou, Y. P.; Yan, H.; Wong, K. S.; Coropceanu, V.; Li, N.; Brabec, C. J.; Bredas, J. L.; Yip, H. L.; Cao, Y. Delocalization of exciton and electron wavefunction in non-fullerene acceptor molecules enables efficient organic solar cells. *Nat. Commun.* **2020**, *11*, 3943.
(28) McMahon, D. P.; Cheung, D. L.; Troisi, A. Why Holes and Electrons Separate So Well in Polymer/Fullerene Photovoltaic Cells. *J. Phys. Chem. Lett.* **2011**, *2*, 2737-2741.
(29) Groves, C. Suppression of geminate charge recombination in organic photovoltaic devices with a cascaded energy heterojunction. *Energy Environ. Sci.* **2013**, *6*, 1546-1551.
(30) Bartelt, J. A.; Beiley, Z. M.; Hoke, E. T.; Mateker, W. R.; Douglas, J. D.; Collins, B. A.; Tumbleston, J. R.; Graham, K. R.; Amassian, A.; Ade, H.; Frechet, J. M. J.; Toney, M. F.; McGehee, M. D. The Importance of Fullerene Percolation in the Mixed Regions of Polymer-Fullerene Bulk Heterojunction Solar Cells. *Adv. Energy Mater.* **2013**, *3*, 364-374.
(31) Westacott, P.; Tumbleston, J. R.; Shoaee, S.; Fearn, S.; Bannock, J. H.; Gilchrist, J. B.; Heutz, S.; deMello, J.; Heeney, M.; Ade, H.; Durrant, J.; McPhail, D. S.; Stingelin, N. On the role of intermixed phases in organic photovoltaic blends. *Energy Environ. Sci.* **2013**, *6*, 2756-2764.
(32) Burke, T. M.; McGehee, M. D. How High Local Charge Carrier Mobility and an Energy Cascade in a Three-Phase Bulk Heterojunction Enable > 90% Quantum Efficiency. *Adv. Mater.* **2014**, *26*, 1923-1928.
(33) Shi, L.; Lee, C. K.; Willard, A. P. The Enhancement of Interfacial Exciton Dissociation by Energetic Disorder Is a Nonequilibrium Effect. *ACS Central Sci.* **2017**, *3*, 1262-1270.

(34) Govatski, J. A.; da Luz, M. G. E.; Koehler, M. Anomalous maximum and minimum for the dissociation of a geminate pair in energetically disordered media. *Chem. Phys. Lett.* **2015**, *620*, 123-128.
(35) Zhu, L. Y.; Zhang, J. Q.; Guo, Y.; Yang, C.; Yi, Y. P.; Wei, Z. X. Small Exciton Binding Energies Enabling Direct Charge Photogeneration Towards Low-Driving-Force Organic Solar Cells. *Angew Chem. Int. Ed.* **2021**, *60*, 15348-15353.
(36) Lee, T. H.; Hillman, S. A. J.; Gonzalez-Carrero, S.; Difilippo, A.; Durrant, J. R. Long-Lived Charges in Y6:PM6 Bulk-Heterojunction Photoanodes with a Polymer Overlayer Improve Photoelectrocatalytic Performance. *Adv. Energy Mater.* **2023**, *13*, 2300400.
(37) Price, M. B.; Hume, P. A.; Ilina, A.; Wagner, I.; Tamming, R. R.; Thorn, K. E.; Jiao, W. T.; Goldingay, A.; Conaghan, P. J.; Lakhwani, G.; Davis, N. J. L. K.; Wang, Y. F.; Xue, P. Y.; Lu, H.; Chen, K.; Zhan, X. W.; Hodgkiss, J. M. Free charge photogeneration in a single component high photovoltaic efficiency organic semiconductor. *Nat. Commun.* **2022**, *13*, 2827.
(38) Wang, R.; Zhang, C. F.; Li, Q.; Zhang, Z. G.; Wang, X. Y.; Xiao, M. Charge Separation from an Intra-Moiety Intermediate State in the High-Performance PM6:Y6 Organic Photovoltaic Blend. *J. Am. Chem. Soc.* **2020**, *142*, 12751-12759.
(39) Jasiunas, R.; Zhang, H. T.; Devizis, A.; Franckevicius, M.; Gao, F.; Gulbinas, V. Thermally Activated Reverse Electron Transfer Limits Carrier Generation Efficiency in PM6:Y6 Non-Fullerene Organic Solar Cells. *Sol. Rrl* **2022**, *6*, 2100963.
(40) Wang, T.; Kafle, T. R.; Kattel, B.; Chan, W.-L. A Multidimensional View of Charge Transfer Excitons at Organic Donor–Acceptor Interfaces. *J. Am. Chem. Soc.* **2017**, *139*, 4098-4106.
(41) Perdigon-Toro, L.; Zhang, H. T.; Markina, A. S.; Yuan, J.; Hosseini, S. M.; Wolff, C. M.; Zuo, G. Z.; Stolterfoht, M.; Zou, Y. P.; Gao, F.; Andrienko, D.; Shoaee, S.; Neher, D. Barrierless Free Charge Generation in the High-Performance PM6:Y6 Bulk Heterojunction Non-Fullerene Solar Cell. *Adv. Mater.* **2020**, *32*, 1906763.
(42) Yao, Y.; Xie, X. Y.; Ma, H. B. Ultrafast Long-Range Charge Separation in Organic Photovoltaics: Promotion by Off-Diagonal Vibronic Couplings and Entropy Increase. *J. Phys. Chem. Lett.* **2016**, *7*, 4830-4835.
(43) Gregg, B. A. Entropy of Charge Separation in Organic Photovoltaic Cells: The Benefit of Higher Dimensionality. *J. Phys. Chem. Lett.* **2011**, *2*, 3013-3015.
(44) Hood, S. N.; Kassal, I. Entropy and Disorder Enable Charge Separation in Organic Solar Cells. *J. Phys. Chem. Lett.* **2016**, *7*, 4495-4500.
(45) Kafle, T. R.; Chan, W. L. Exciton Heating Versus Cooling: Charge Separation Driven by Entropy and Delocalization at Interfaces with Planar Molecules. *Phys. Rev. Appl.* **2021**, *15*, 044054.
(46) Kafle, T. R.; Kattel, B.; Wanigasekara, S.; Wang, T.; Chan, W. L. Spontaneous Exciton Dissociation at Organic Semiconductor Interfaces Facilitated by the Orientation of the Delocalized Electron-Hole Wavefunction. *Adv. Energy Mater.* **2020**, *10*, 1904013.
(47) Neusser, D.; Sun, B. W.; Tan, W. L.; Thomsen, L.; Schultz, T.; Perdigón-Toro, L.; Koch, N.; Shoaee, S.; McNeill, C. R.; Neher, D.; Ludwigs, S. Spectroelectrochemically determined energy levels of PM6:Y6 blends and their relevance to solar cell performance. *J. Mater. Chem. C* **2022**, *10*, 11565-11578.
(48) Li, X. E.; Zhang, Q. L.; Yu, J. W.; Xu, Y.; Zhang, R.; Wang, C. F.; Zhang, H. T.; Fabiano, S.; Liu, X. J.; Hou, J. H.; Gao, F.; Fahlman, M. Mapping the energy level alignment at donor/acceptor interfaces in non-fullerene organic solar cells. *Nat. Commun.* **2022**, *13*, 2046.

(49) Bertrandie, J.; Han, J. H.; De Castro, C. S. P.; Yengel, E.; Gorenflot, J.; Anthopoulos, T.; Laquai, F.; Sharma, A.; Baran, D. The Energy Level Conundrum of Organic Semiconductors in Solar Cells. *Adv. Mater.* **2022**, *34*, 2202575.
(50) Ishii, H.; Sugiyama, K.; Ito, E.; Seki, K. Energy level alignment and interfacial electronic structures at organic metal and organic organic interfaces. *Adv. Mater.* **1999**, *11*, 605-625.
(51) Karuthedath, S.; Gorenflot, J.; Firdaus, Y.; Chaturvedi, N.; De Castro, C. S. P.; Harrison, G. T.; Khan, J. I.; Markina, A.; Balawi, A. H.; Pena, T. A. D.; Liu, W.; Liang, R. Z.; Sharma, A.; Paleti, S. H. K.; Zhang, W.; Lin, Y.; Alarousu, E.; Lopatin, S.; Anjum, D. H.; Beaujuge, P. M.; De Wolf, S.; McCulloch, I.; Anthopoulos, T. D.; Baran, D.; Andrienko, D.; Laquai, F. Intrinsic efficiency limits in low-bandgap non-fullerene acceptor organic solar cells. *Nat Mater* **2021**, *20*, 378-384.
(52) Shoaee, S.; Luong, H. M.; Song, J. G.; Zou, Y. P.; Nguyen, T. Q.; Neher, D. What We have Learnt from PM6:Y6. *Adv. Mater.* **2023**, 2302005.
(53) Tu, S. L.; Zhang, L.; Lin, X.; Xiao, L. R.; Wang, W.; Ling, Q. D. Modifying polymer PM6 by incorporating a third component for an enhanced short-circuit current density. *J. Mater. Chem. C* **2022**, *10*, 2026-2033.
(54) Kafle, T. R.; Kattel, B.; Yao, P.; Zereshki, P.; Zhao, H.; Chan, W. L. Effect of the Interfacial Energy Landscape on Photoinduced Charge Generation at the ZnPc/MoS2 Interface. *J. Am. Chem. Soc.* **2019**, *141*, 11328-11336.
(55) Xie, Y. P.; Cai, Y. H.; Zhu, L.; Xia, R. X.; Ye, L. L.; Feng, X.; Yip, H. L.; Liu, F.; Lu, G. H.; Tan, S. T.; Sun, Y. M. Fibril Network Strategy Enables High-Performance Semitransparent Organic Solar Cells. *Adv. Funct. Mater.* **2020**, *30*, 2002181.
(56) Yao, N. N.; Wang, J. Q.; Chen, Z.; Bian, Q. Z.; Xia, Y. X.; Zhang, R.; Zhang, J. Q.; Qin, L. Q.; Zhu, H. M.; Zhang, Y.; Zhang, F. L. Efficient Charge Transport Enables High Efficiency in Dilute Donor Organic Solar Cells. *J. Phys. Chem. Lett.* **2021**, *12*, 5039-5044.
(57) Zhang, X. N.; Li, C.; Xu, J. Q.; Wang, R.; Song, J. L.; Zhang, H.; Li, Y. X.; Jing, Y. N.; Li, S. L.; Wu, G. B.; Zhou, J.; Li, X.; Zhang, Y. Y.; Li, X.; Zhang, J. Q.; Zhang, C. F.; Zhou, H. Q.; Sun, Y. M.; Zhang, Y. High fill factor organic solar cells with increased dielectric constant and molecular packing density. *Joule* **2022**, *6*, 444-457.
(58) Yao, Y. Establishing a microscopic model for nonfullerene organic solar cells: Self-accumulation effect of charges. *J. Chem. Phys.* **2018**, *149*, 194902.
(59) Kafle, T. R.; Wang, T.; Kattel, B.; Liu, Q.; Gong, Y.; Wu, J.; Chan, W.-L. Hot Exciton Relaxation and Exciton Trapping in Single-Walled Carbon Nanotube Thin Films. *J. Phys. Chem. C* **2016**, *120*, 24482-24490.
(60) Wang, T.; Chan, W. L. Dynamical Localization Limiting the Coherent Transport Range of Excitons in Organic Crystals. *J. Phys. Chem. Lett.* **2014**, *5*, 1812-1818.
(61) Rudayni, F., Rijal K., Fuller N., Chan, W. -L. . Enthalpy-Uphill Exciton Dissociation at Organic/2D Heterostructures Promotes Free Carrier Generation. *Materials Horizons* **2024**, *in-press*, 10.1039/D1033MH01522J.
(62) Kafle, T. R.; Kattel, B.; Wang, T.; Chan, W.-L. The relationship between the coherent size, binding energy and dissociation dynamics of charge transfer excitons at organic interfaces. *J. Phys.: Condens. Matter* **2018**, *30*, 454001.
(63) Chen, H. Y.; Hu, D. Q.; Yang, Q. G.; Gao, J.; Fu, J. H.; Yang, K.; He, H.; Chen, S. S.; Kan, Z. P.; Duan, T. N.; Yang, C.; Ouyang, J. Y.; Xiao, Z. Y.; Sun, K.; Lu, S. R. All-Small-Molecule Organic Solar Cells with an Ordered Liquid Crystalline Donor. *Joule* **2019**, *3*, 3034-3047.

(64) Kerremans, R.; Kaiser, C.; Li, W.; Zarrabi, N.; Meredith, P.; Armin, A. The Optical Constants of Solution-Processed Semiconductors—New Challenges with Perovskites and Non-Fullerene Acceptors. *Adv. Opt. Mater.* **2020**, *8*, 2000319.

Supporting Information

Endothermic Charge Separation Occurs Spontaneously in Non-Fullerene Acceptor/Polymer Bulk Heterojunction

Kushal Rijal,[1,*] Neno Fuller,[1] Fatimah Rudayni,[1,2] Nan Zhang,[3] Xiaobing Zuo,[4] Cindy L. Berrie,[5] Hin-Lap Yip,[3,6,7] Wai-Lun Chan[1,*]

1. Department of Physics and Astronomy, University of Kansas, Lawrence, Kansas 66045, USA
2. Department of Physics, Jazan University, Jazan 45142, Saudi Arabia
3. Department of Materials Science and Engineering, City University of Hong Kong, Tat Chee Avenue, Kowloon, Hong Kong
4. X-ray Science Division, Argonne National Laboratory, Lemont, Illinois 60439, USA
5. Department of Chemistry, University of Kansas, Lawrence, Kansas 66045, USA
6. School of Energy and Environment, City University of Hong Kong, Tat Chee Avenue, Kowloon, Hong Kong
7. Hong Kong Institute for Clean Energy, City University of Hong Kong, Tat Chee Avenue, Kowloon, Hong Kong

[*]Email: kushalko85@ku.edu, wlchan@ku.edu

I. Additional UPS spectra

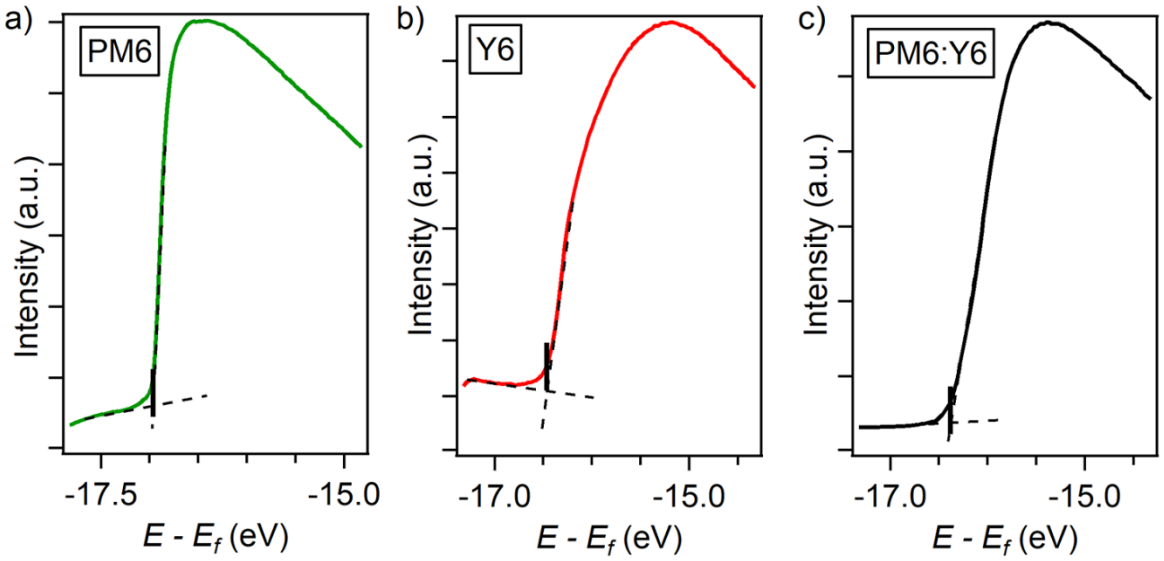

Fig. S1: The UPS spectra for (a) PM6, (b) Y6, and (c) PM6:Y6 blend films near the SECO region. The SECO position for each spectrum is indicated by the solid black line.

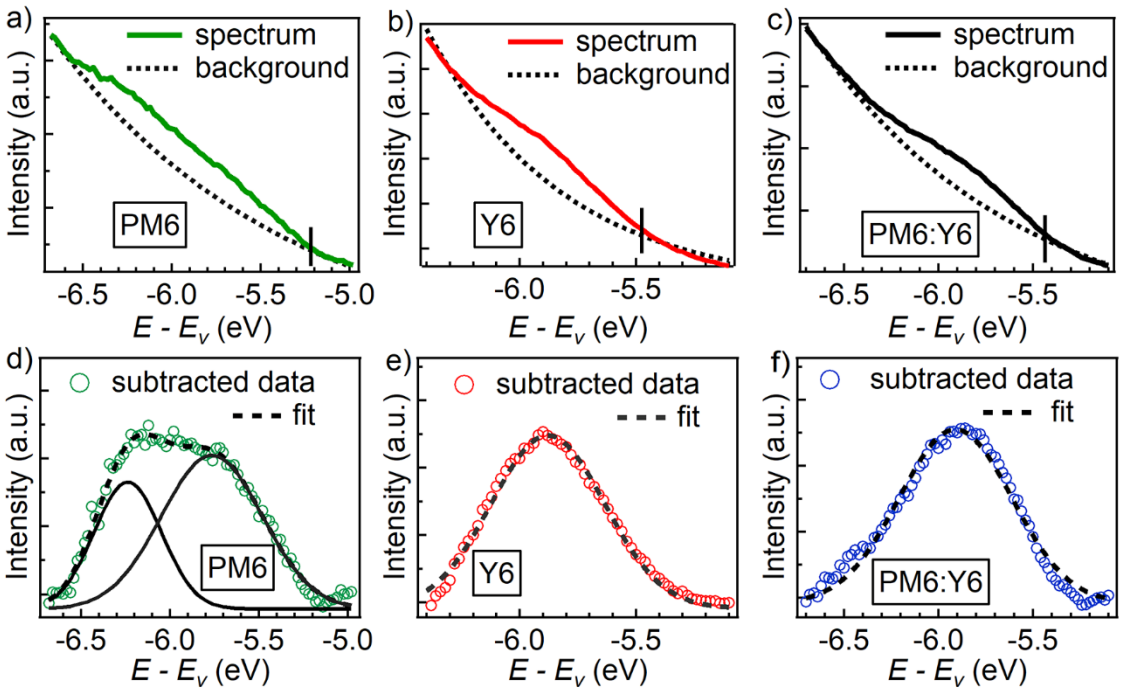

Fig. S2: The HOMO peak of (a & d) PM6, (b & e) Y6 and (c & f) PM6:Y6 blend. The energy is referenced with respect to the vacuum level (E_v). The dotted curves in a, b & c represent the background originated from inelastic photoelectrons. The HOMO-edge positions are labelled in Fig. S2 (a-c) by vertical bars. These edge positions are used to determine the ionization potential. To determine the HOMO peak position, we substract the background from the raw spectrum. The subtracted data and the gaussian fits are shown in d, e & f. The gaussian peak obtained from the fits corresponds to the HOMO (peak) level for each film. For PM6, two peaks are found. The higher energy peak is taken as the HOMO.

Sample	**Work function**	**HOMO (edge) from E_v**	**Ionization potential**	**HOMO (peak) from E_v**	**Lowest Optical Absorption peak**
PM6	4.26 eV	-5.22 eV	5.22 eV	-5.76 eV	615 nm (2.02 eV)
Y6	4.76 eV	-5.48 eV	5.48 eV	-5.88 eV	836 nm (1.48 eV)
PM6:Y6 blend	4.86 eV	-5.44 eV	5.44 eV	-5.91 eV	822 nm (1.51 eV)

Table S1: A summary for work function, ionization potentials, HOMO positions and optical bandgap for all samples.

II. Additional TR-TPPE data

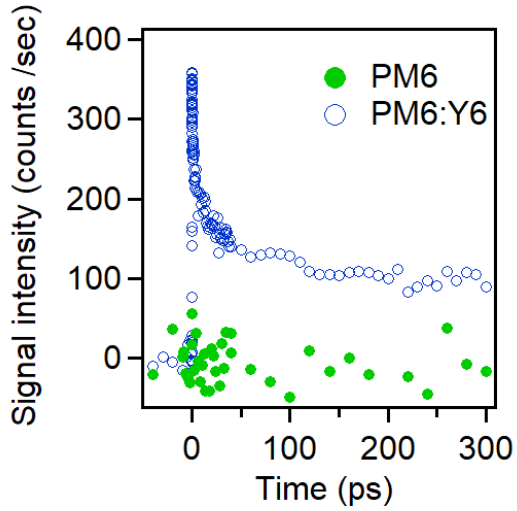

Fig. S3: (a) TR-TPPE signal (integrated across all energies) from PM6 and PM6:Y6 blend films collected with the 780-nm pump excitation. We cannot obtain any pump-induced TPPE signal from the neat PM6 film.

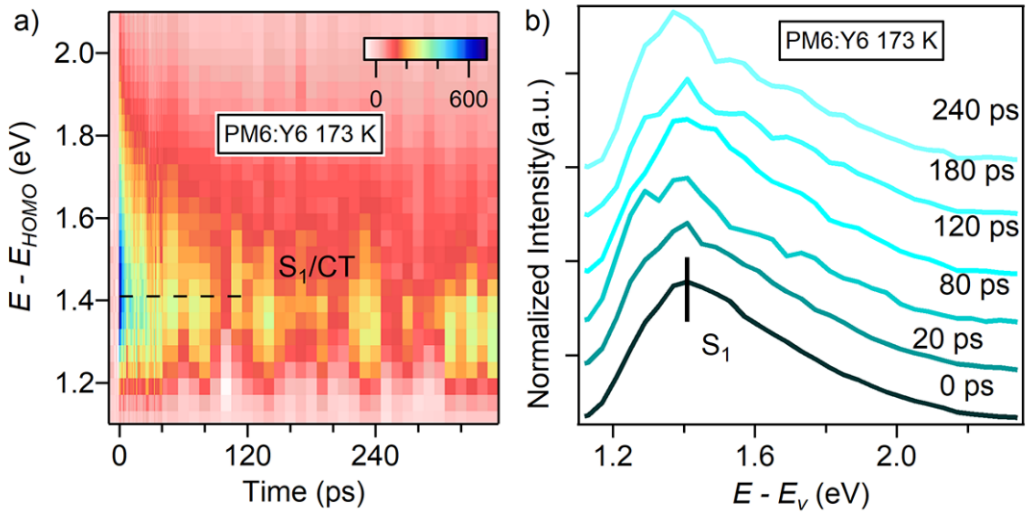

Fig. S4: (a) The TR-TPPE spectrum of PM6:Y6 blend collected at 173 K. No energy uphill CS is observed. (b) Vertical cut of the TR-TPPE spectra at different delay times.

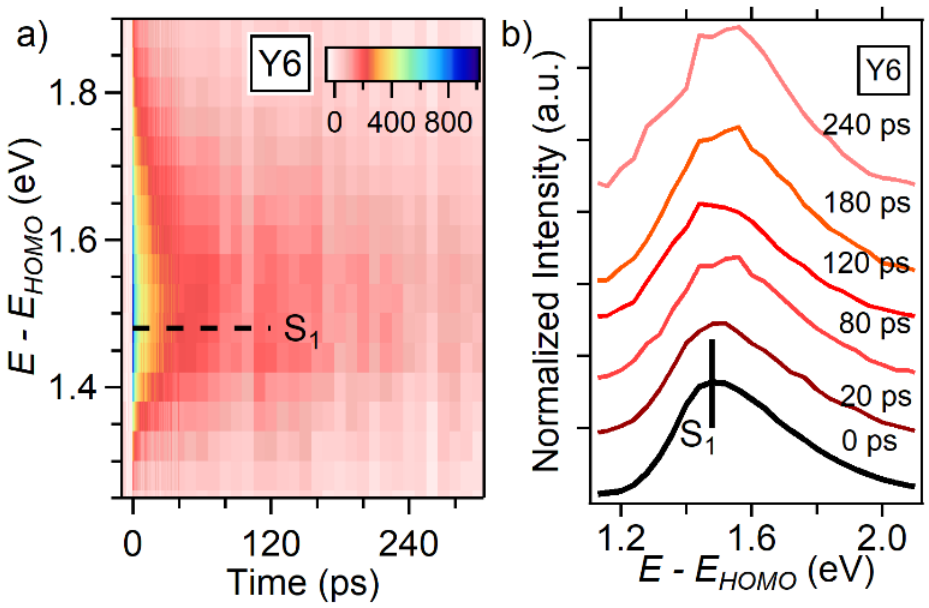

Fig. S5: (a) TR-TPPE spectrum of Y6 film collected at room temperature with a pump wavelength of 780nm. Population in S_1 states continuously decays throughout the time. No energy uphill CS is observed. (b) Vertical cuts of the spectra from (a) at different time delays.

III. "Peak-to-peak" versus "Edge-to-edge" method in determining exciton energy.

The edge of the HOMO peak and the edge of the LUMO peak are often used in UPS-inverse photoemission spectroscopy (IPES) studies to estimate the transport gap. In the case of UPS-IPES, it is known that the peak-to-peak separation overestimates the transport gap because of opposite polarization effects.[S1, 2] In UPS (IPES) experiment, an electron is removed (added) to the surface, which forms a positively-charged (negatively-charged) polarization cloud on the surface. The polarization effect shifts the UPS and IPES spectra in opposite direction, and can overestimate the bandgap for organic materials by as much as ~ 0.8 eV.[S1, 2] Hence, the edge-to-edge method is traditionally used to "correct" for this overestimation.[S1] In our case, TPPE instead of IPES is used to probe the excited state. In contrary to IPES, electrons are removed from the surface in the TPPE experiment. Hence, the polarization effect will shift the TPPE and UPS spectra in the same direction, which creates much less effect on the energy separation between a UPS peak and a TPPE peak. Therefore, it is more appropriate to use the peak-to-peak separation for finding the exciton energy from a pair of UPS and TPPE spectra. Moreover, for optical excitations, states with the highest density of state (peak) instead of band edge states are primarily excited by the pump pulse, and excited electrons take time to relax to the band edge (see, e.g. Fig. 3 in the main text). These reasons also justify the use of peak positions for determining exciton energies. The same method has been previously employed us[S3-7] and others[S8] to estimate the exciton energy from UPS and TPPE spectra.

IV. Derivation of Eq. (2) in the main text

The binding energy of Y6's S_1 exciton (Ex_b^{S1}) and the CT exciton (Ex_b^{CT}) can be written as:

$$Ex_b^{S1} = (E_{LUMO}^{Y6} - E_{HOMO}^{Y6}) - E_{S1}^{Y6}, \text{ and} \quad \text{(S1)}$$

$$Ex_b^{CT} = (E_{LUMO}^{Y6} - E_{HOMO}^{PM6}) - E_{CT}. \quad \text{(S2)}$$

In these two equations, E_{LUMO}^{Y6}, E_{HOMO}^{Y6}, and E_{HOMO}^{PM6} are the Y6's LUMO, Y6's HOMO and PM6's HOMO energies, respectively. E_{S1}^{Y6} and E_{CT} are the energy of the Y6's S_1 exciton and the energy of the CT exciton, respectively.

Subtracting Eq. (S2) and (S1), we can get the difference between the two binding energies:

$$Ex_b^{S1-CT} = Ex_b^{S1} - Ex_b^{CT} = (E_{HOMO}^{PM6} - E_{HOMO}^{Y6}) - (E_{S1}^{Y6} - E_{CT}), \quad \text{(S3)}$$

which is same as the Eq. (2) in the main text.

V. Time-resolved photoluminescence (TR-PL) measurements

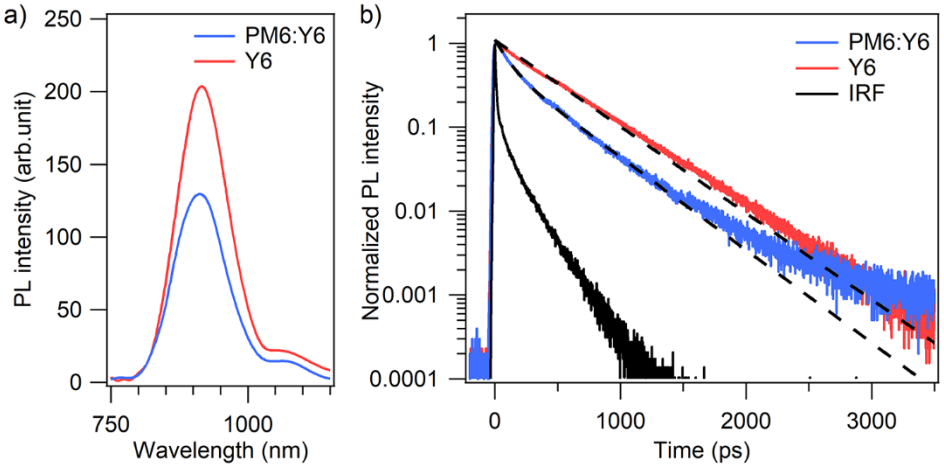

Fig. S6: (a) Time-integrated PL spectra of PM6:Y6 and neat Y6 films. (b) Integrated PL intensity as a function of time for PM6:Y6 and neat Y6 films. All the curves are normalized to 1 at $t \sim 0$. The data for the PM6:Y6 is fit to a bi-exponential function, while the data for the Y6 is fit to a mono-exponential function. Fits are shown as dashed line. The IRF in the figure caption represents instrumental response function.

Film	**A_1**	**τ_1**	**A_2**	**τ_2**
PM6:Y6	48 %	105 ps	52 %	393 ps
Y6	100 %	421 ps	-	-

Table S2: A summary of parameters obtained from the fit.

VI. Additional X-ray scattering data and fitting

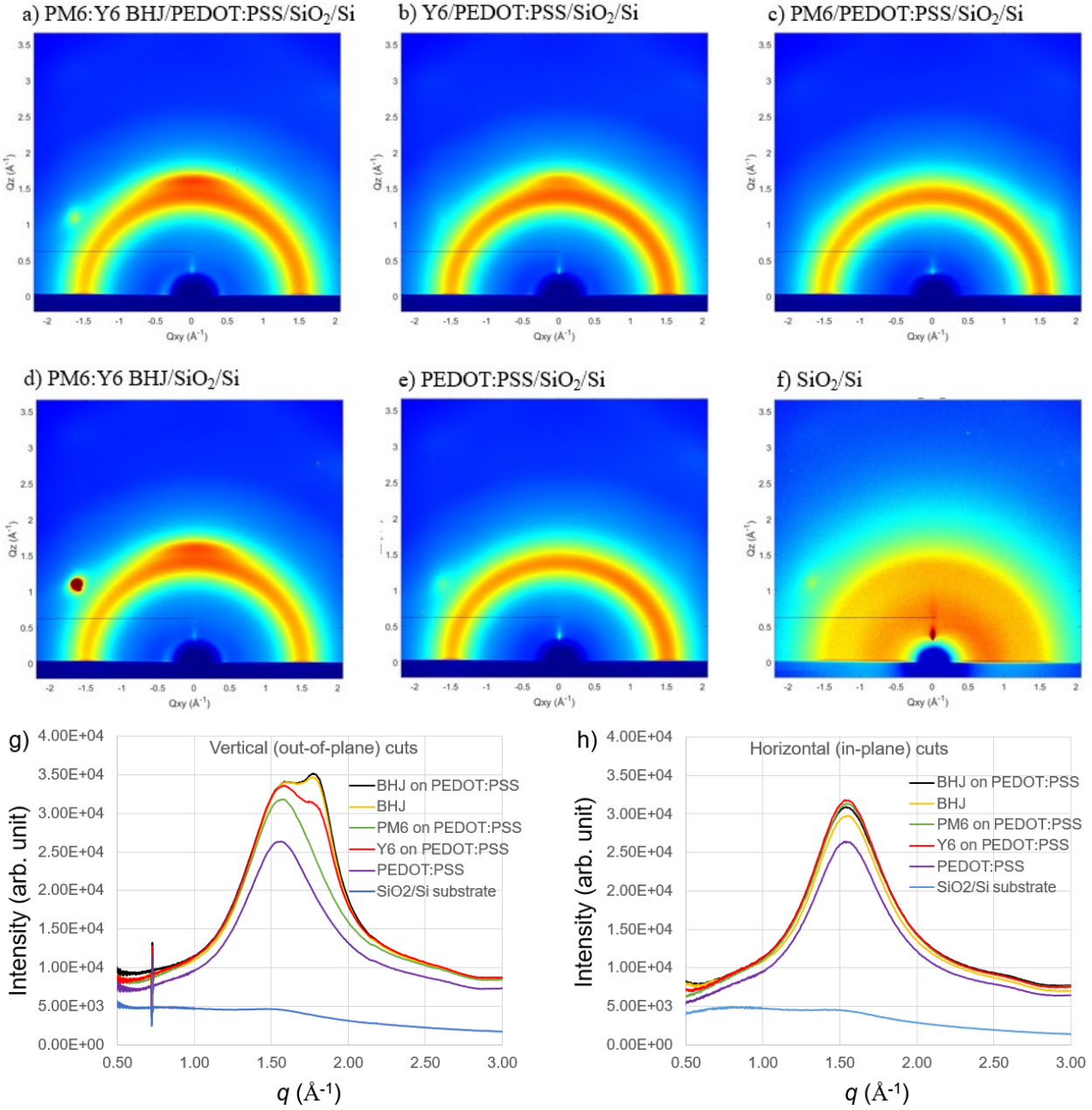

Fig. S7: The GIWAXS patterns of (a) PM6:Y6 BHJ/PEDOT:PSS/SiO_2/Si, (b) Y6/PEDOT:PSS/SiO2/Si, (c) PM6/PEDOT:PSS/SiO_2/Si, (d) PM6:Y6 BHJ/SiO_2/Si, (e) PEDOT:PSS/SiO_2/Si, and (f) SiO_2/Si samples. The vertical (out-of-plane) and horizontal (in-plane) cuts of these GIWAXS patterns ((a) to (f)) are shown in (g) and (h), respectively.

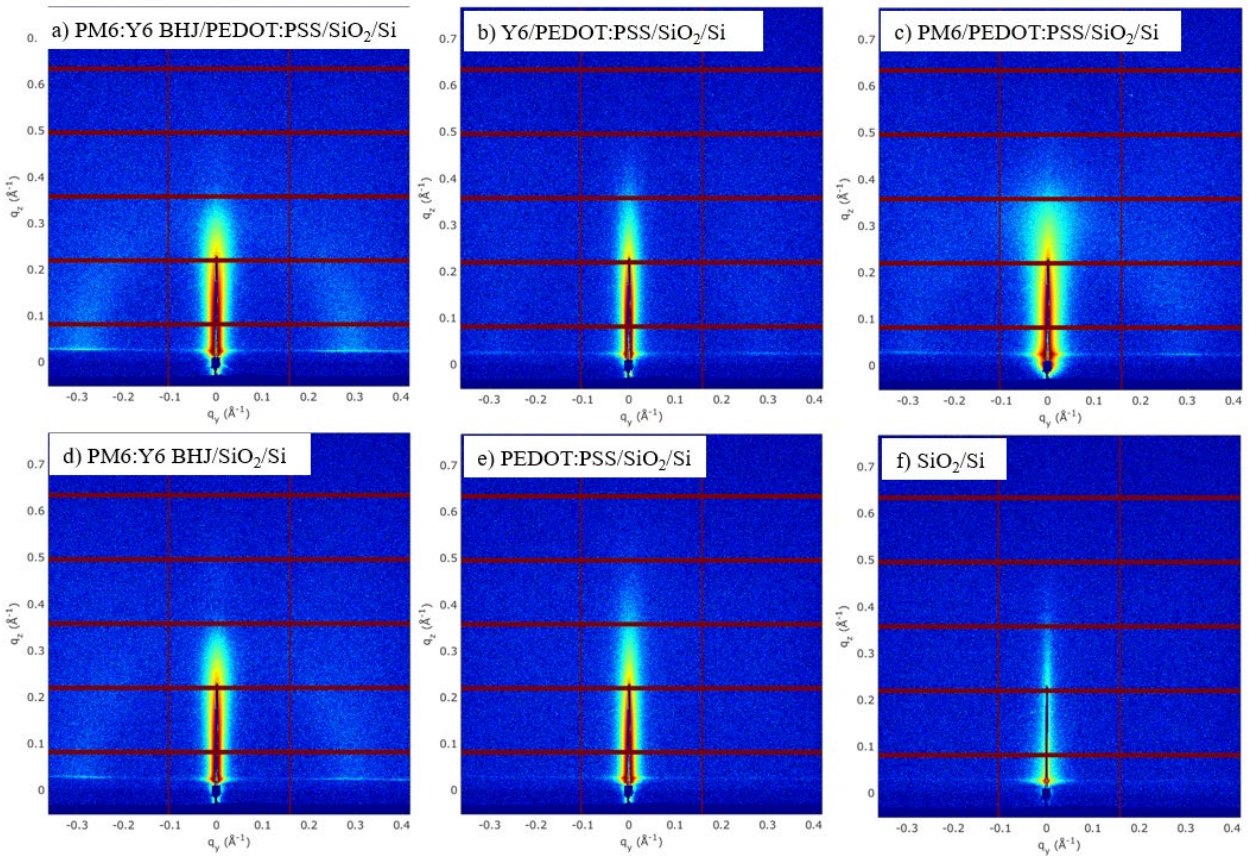

Fig. S8: The GISAXS patterns of (a) PM6:Y6 BHJ/PEDOT:PSS/SiO_2/Si, (b) Y6/PEDOT:PSS/SiO2/Si, (c) PM6/PEDOT:PSS/SiO_2/Si, (d) PM6:Y6 BHJ/SiO_2/Si, (e) PEDOT:PSS/SiO_2/Si, and (f) SiO_2/Si samples.

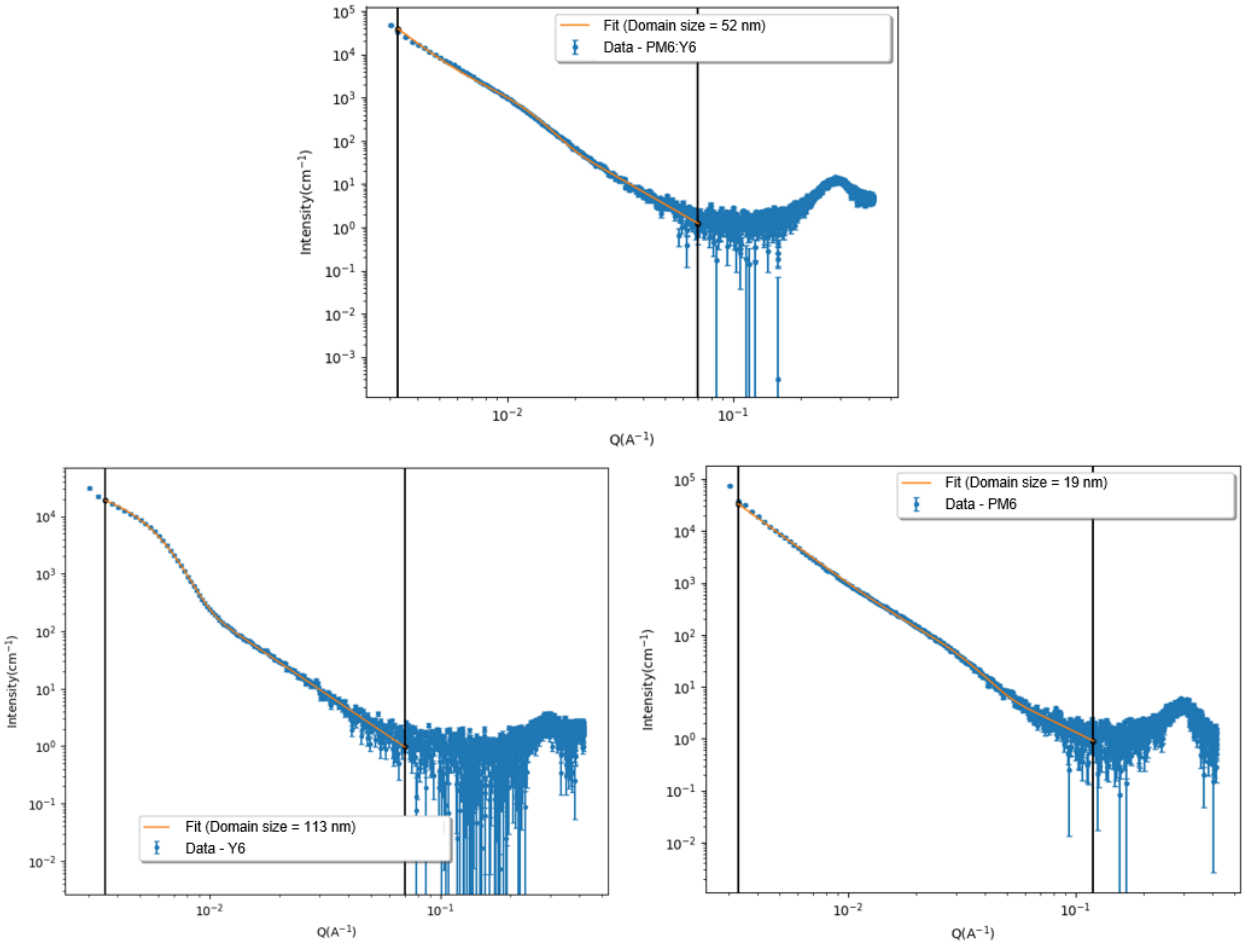

Fig. S9: Fits for the GISAXS horizontal linecut for the PM6:Y6, Y6, and PM6 samples. The background of the substrate was first subtracted from sample GISAXS linecuts. Then, they are fitted with SAXS unified model[S9] using program SasView [https://www.sasview.org/]. The domain size was estimated using the R_g value obtained from unified model fitting and the sphere shape approximation.

VII. Additional AFM data

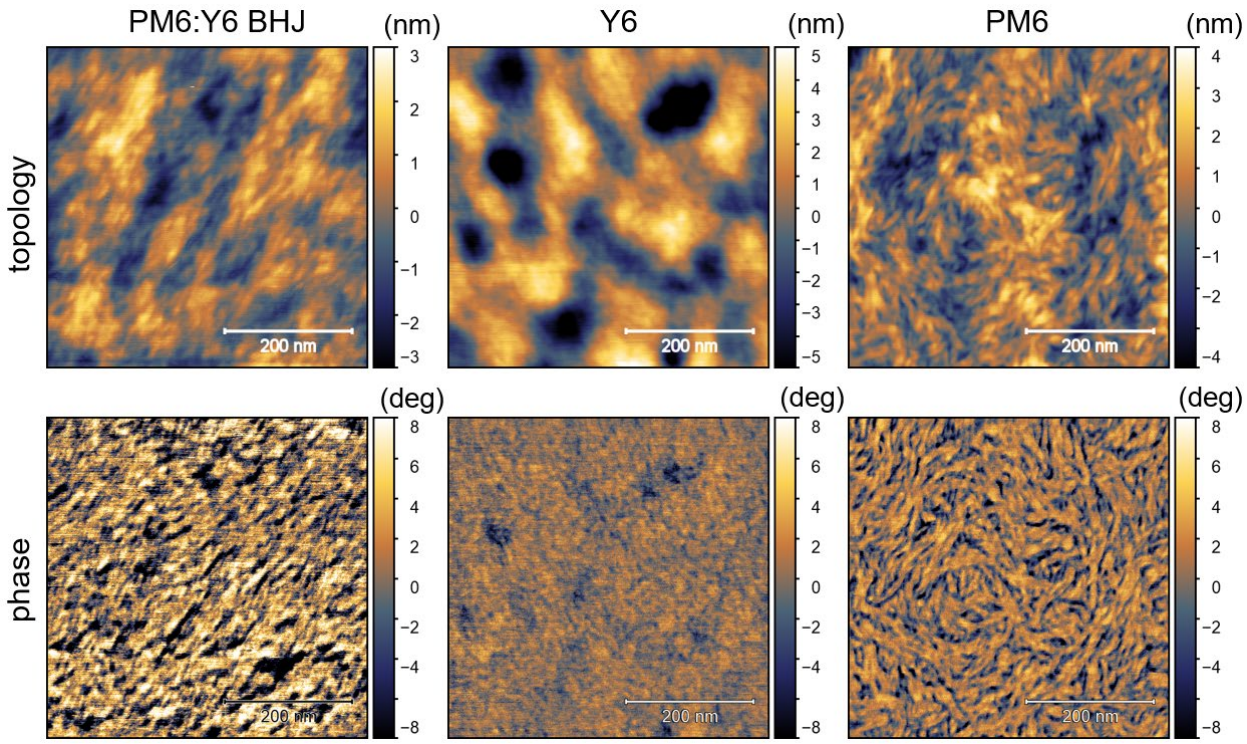

Fig. S10: The topology and phase images of PM6:Y6 BHJ, Y6 and PM6 samples.

VIII. Estimation of the excitation density

The excitation density (ρ) was estimated using the following formula:

$$\rho = \frac{J \times \alpha \times (1 - R)}{h\upsilon}$$

, where J, α, R, and $h\upsilon$ are the incident fluence of the pump pulse, optical absorption constant, reflectivity, and the pump photon energy, respectively. In our experiment, for an incidence angle of 30º, J was 10.15 μJ cm^{-2}. The central wavelength of the pump pulse λ was 780 nm. At this wavelength, the attenuation coefficient, and the refractive index of the PM6:Y6 film were taken to be $k \approx 1.2$, and $n \approx 2.2$ respectively. Note that the mixing ratio of our PM6:Y6 BHJ sample is (1:3). To arrive at the above n and k, we took the averaged values of n and k for the neat-Y6 and PM6:Y6 (1:1.2) reported in Ref. 64 cited in the main text.

The absorption constant α was calculated using the formula:

$$\alpha = \frac{4\pi \times \ k}{\lambda}$$

The α at 780 nm is calculated to be 1.93×10^5 cm^{-1}.

R was calculated using the Fresnel equation (for p-polarized light) [Ref. S10]:

$$R = \left| \frac{{n_2}^2 \cos\theta - n_1\sqrt{{n_2}^2 - (n_1 \sin\theta)^2}}{{n_2}^2 \cos\theta + n_1\sqrt{{n_2}^2 - (n_1 \sin\theta)^2}} \right|^2$$

,where θ = 30° is the angle of incidence, n_1 =1 is the refractive index of the incident medium (vacuum), and $n_2 = n + ik$ is the complex refractive index of the organic film.

The calculated R is 0.2.

Using the above equations, we estimate that ρ ~ 6.2×10^{18} cm^{-3}.

References

(S1) Zahn, D. R. T.; Gavrila, G. N.; Gorgoi, M. The transport gap of organic semiconductors studied using the combination of direct and inverse photoemission. *Chem. Phys.* **2006**, *325*, 99-112.

(S2) Hill, I. G.; Kahn, A.; Soos, Z. G.; Pascal, R. A. Charge-separation energy in films of pi-conjugated organic molecules. *Chem. Phys. Lett.* **2000**, *327*, 181-188.

(S3) Kafle, T. R.; Kattel, B.; Yao, P.; Zereshki, P.; Zhao, H.; Chan, W. L. Effect of the Interfacial Energy Landscape on Photoinduced Charge Generation at the ZnPc/MoS2 Interface. *J. Am. Chem. Soc.* **2019**, *141*, 11328-11336.

(S4) Wang, T.; Kafle, T. R.; Kattel, B.; Chan, W.-L. A Multidimensional View of Charge Transfer Excitons at Organic Donor–Acceptor Interfaces. *J. Am. Chem. Soc.* **2017**, *139*, 4098-4106.

(S5) Kafle, T. R.; Kattel, B.; Lane, S. D.; Wang, T.; Zhao, H.; Chan, W. L. Charge Transfer Exciton and Spin Flipping at Organic-Transition-Metal Dichalcogenide Interfaces. *ACS Nano* **2017**, *11*, 10184-10192.

(S6) Kafle, T. R.; Chan, W. L. Exciton Heating Versus Cooling: Charge Separation Driven by Entropy and Delocalization at Interfaces with Planar Molecules. *Phys. Rev. Appl.* **2021**, *15*, 044054.

(S7) Wang, T.; Chan, W. L. Dynamical Localization Limiting the Coherent Transport Range of Excitons in Organic Crystals. *J. Phys. Chem. Lett.* **2014**, *5*, 1812-1818.

(S8) Man, M. K. L.; Madeo, J.; Sahoo, C.; Xie, K. C.; Campbell, M.; Pareek, V.; Karmakar, A.; Wong, E. L.; Al-Mahboob, A.; Chan, N. S.; Bacon, D. R.; Zhu, X.; Abdelrasoul, M. M. M.; Li, X. Q.; Heinz, T. F.; da Jornada, F. H.; Cao, T.; Dani, K. M. Experimental measurement of the intrinsic excitonic wave function. *Sci. Adv.* **2021**, *7*, eabg0192.

(S9) Beaucage, G. (2012). Combined Small-Angle Scattering for Characterization of Hierarchically Structured Polymer Systems over Nano-to-Micron Meter: Part II Theory. In Polymer Science: A Comprehensive Reference (M, MKaM, ed.), Vol. 2, pp. 399. Elsevier, Amsterdam.

(S10) Jackson, J. D. (1998). Classical Electrodynamics, Third Edition, pp. 306. John Wiley & Sons, Inc., New York.